UiO : Department of Mathematics
University of Oslo

Modeling the effect of slits on rowing blades

A numerical investigation

Sverre Vinje

Master's Thesis, Spring 2022

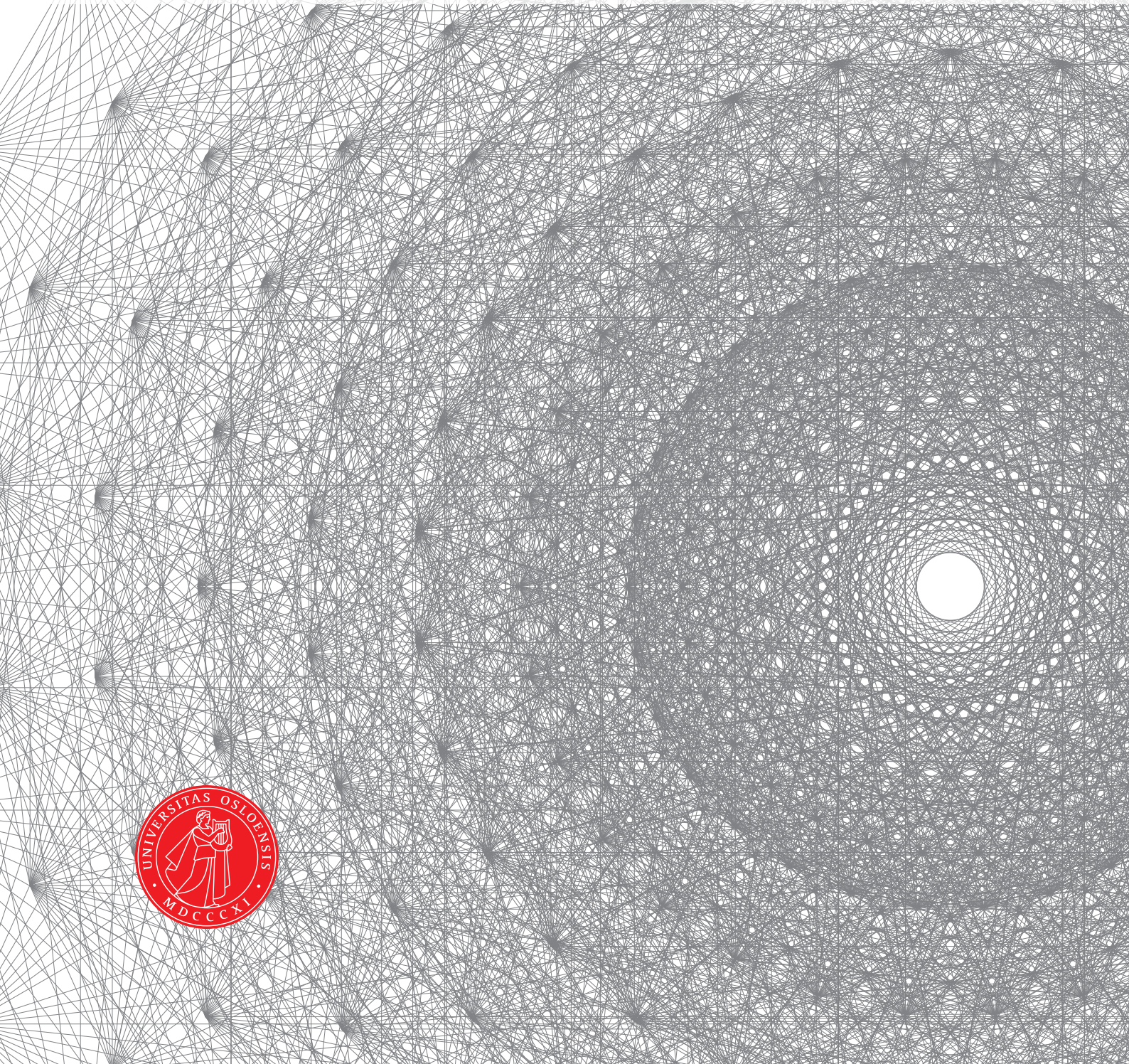

This master's thesis is submitted under the master's programme *Mechanics*, with programme option *Mechanics*, at the Department of Mathematics, University of Oslo. The scope of the thesis is 60 credits.

The front page depicts a section of the root system of the exceptional Lie group E_8, projected into the plane. Lie groups were invented by the Norwegian mathematician Sophus Lie (1842–1899) to express symmetries in differential equations and today they play a central role in various parts of mathematics.

Abstract

Rowing is a sport where the objective is to get as fast as possible from point A to point B, using a boat, oars and human forces. A major interest for rowers is how to optimize the equipment to increase boat speed, and in particular increase drag and lift coefficients of the rowing blade. A rowing blade design called Oscar Blades is a blade that consists of multiple narrow slits. It is hypothesized by the manufacturer of these blades that the slits will increase propulsion.

The current study has investigates whether slits on rowing blades can increase propulsive efficiency by evaluating how the slits affect the drag and lift coefficients C_D and C_L through the usage of CFD modeling. The blade geometry was created using the open source platform SALOME, and the corresponding computational meshes were created with cfMesh. Finally, velocity and pressure fields around the blades were computed in OpenFOAM.

We found that blades with the slit configurations tested in this study substantially reduced the lift coefficient with increased open area. The drag coefficients displayed lower variability between different configurations, but did not generally increase with open area.

Despite promising results on how to increase drag from other sports (e.g. swimming) the results from the present study do not advocate for the inclusion of slits in rowing blades. However, testing on more blade and slit configurations is needed to add certainty to the present study.

Acknowledgements

First and foremost I would like to thank my main supervisor Atle Jensen and my co-supervisor Mikeal Mortensen for their guidance through this project. I have enjoyed our weekly meetings and appreciate the consistent follow-up provided. Additionally I am grateful for being assigned with a very suitable topic given my background as a rower.

I would like to thank everyone in study room 901 for contributing to a very fun and engaging environment. This includes Philip, Sophus, Tov, Jouval, Jonas, Marie, Jakob L, May-Iren, Jakob H, Eva and Lars.

Finally I would like to thank my father and my brothers for giving me feedback and encouragement. This was very helpful. I am lucky to have a very supporting family around me.

Contents

List of Figures

List of Tables

CHAPTER 1

Related research

1.1 Introduction

Increasing the boat speed is the main thing a competitive rower is concerned about. There are two fundamental factors that affect the boat speed: physiological factors and equipment. The focus on this thesis is on the equipment, specifically the rowing blades. The blade manufacturer Oscar Propulsion has hypothesized that slits on the rowing blade can increase thrust generated and thus result in higher boat speed. One justification made for this hypothesis is that in swimming, finger spacing is often advised and is believed to increase thrust based upon the scientific literature (Houwelingen et al. 2017; Minetti, Machtsiras and Masters 2009). The question then is: can the same logic be applied to rowing blades? Will slits on rowing blades, being analogous to finger spacing in swimming, increase the propulsive force? Experimental studies have aimed to understand fluid mechiancis related to the rowing stroke (Caplan and T. N. Gardner 2007; Grift, Tummers and Westerweel 2021), but experimental testing may be expensive and require additional investment to test small changes in blade geometry. An alternative approach is to study blade drag and lift coefficients with computational fluid dynamics (CFD). Some attempts have been made in the literature (Coppel et al. 2010; Robert, Leroyer, Barré, Queutey et al. 2019; Sliasas and Tullis 2009), but blades with slits have not been investigated in this context.

In this thesis, we will therefore investigate drag and lift coefficients for different blade configurations with and without slits. These coefficients, which are associated with the propulsive force, will be compared between the different blades.

In the rest of this chapter, the basic mechanisms of rowing will be outlined. In addition, some relevant research on oar blades and the literature on finger spacing will be reviewed.

1.2 What is rowing?

Rowing is a discipline stemming back from ancient times as means of transportation across lakes, rivers and oceans. Modern rowing competitions, called regattas, traces back to the River Thames i London. It started gaining traction throughout the 19th century, and in 1900 it was endorsed as an Olympic event (Secher and Volianitis 2009). Since then, the sport has seen a significant growth in popularity and is currently practised worldwide. Since the time of it's Olympic debut, the equipment has been continuously modified and developed to optimize the hydrodynamics for greater boat speed. This, combined with developments in training regimes has resulted in significant reductions in winning times throughout rowing's competitive history, with the latest fastest time in men's single sculls recorded in 2017 (as of April 2022).

Modern rowing is divided into two categories; *sculling* and *sweeping*. Sculling is where the rower has two oars; one in each hand, and sweeping is where the rower only has one oar. There are six boat classes included in the Olympic games: single, double and quadruple scull within the sculling category, and pair, four and eight within the sweeping category. The average boat speed in a 2000 m race for top Olympic athletes varies between approximately 4 ms^{-1} to 6.8 ms^{-1}, depending on boat category, sex and weather conditions.

Figure 1.1: Picture of a rower in a single scull. Picture taken by Estela Re-Ma.

1.3 The physics of rowing

Propulsion in rowing is done by applying force to the oar handle, which then is transferred to the oar blade, resulting in the boat moving forward. The full movement of rowing is cyclic and can be divided into four phases (Kleshnev 2020):

Catch: The rower is fully leaned forward with compressed legs and inserts the blade into the water.
Drive: Force is applied to the handle by the rower extending his/her legs, rotating their trunk and pulling the handle. This is also referred to as the *working phase* of the stroke.
Finish: Drive phase is finished, and the rower lifts the blades by pushing the handles downward, while also rotating the handle to re-position the blade to a parallel position relative to the water surface.
Recovery: The rower rotates the trunk and compresses their legs. This is preparation for inserting the oar blades into the water. The blade is kept approximately parallel to the water surface during the start of this phase, but is rotated by the rower from the handle such that the blade is positioned normal to the water surface before the catch.

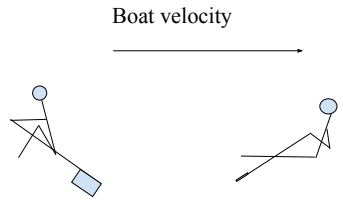

Figure 1.2: Side view of the rower during the catch and finish phase of the stroke.

1.3.1 Shell velocity

The velocity of a rowing boat throughout a full cycle of the rowing stroke is not constant. The main structure of a competitive rowing boat is referred to as the *shell* of the boat. The rower is placed on a sliding seat, and the rower does not move in phase with the velocity of the shell. During the recovery phase the rower moves in the opposite direction relative to the shell, while during the drive the rower moves with the shell. The mass of the rower is generally much greater than that of the shell which makes the rowers motion on the shell's instantaneous velocity significant. Through measurements, Martin and Bernfield (1980) found that the average deviation from mean shell velocity was -24.4% and $+18.6\%$ measured from six trials at 37, 39 and 41 strokes per minute in an eight. Additionaly, they found that the maximal shell velocity during the cycle occurs directly before the catch, while the lowest velocity occurs at the beginning of the drive. Other studies have later confirmed these findings (Caplan and T. Gardner 2007), and additionally showing that shell

velocity deviation is higher in a double compared to an eight (Baudouin and Hawkins 2004).

1.3.2 Oar blade dynamics

From the catch and through to the finish, the blade rotates around the vertical axis, and this movement sheds vortices through the different angles α, where α indicates the angle between the boat shell and the oar (shown in Figure 1.3). These vortices affects the forces on the blade through the movement (Pulman 2005). The complexity of the blade kinematics and the hydrodynamics of the vortices makes it difficult to do realistic field and force calculations without closely replicating the blade movement.

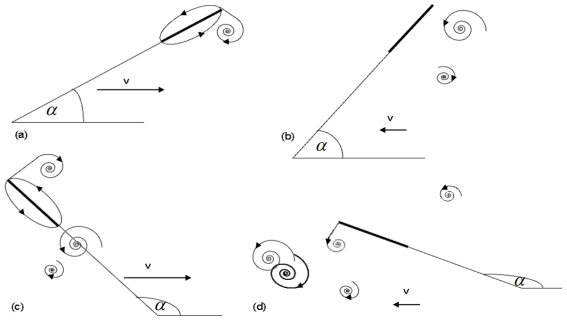

Figure 1.3: The formation of vortices through the stroke for different angles α between oar and shell. Illustration from Pulman (2005).

In addition to rotation, the blade undergoes a slight translation further away from the shell during the drive phase as the oar angles increases to $\alpha = 90°$. The exact path of the blade has been measured (Kleshnev 1999) and is indicated in Figure 1.4.

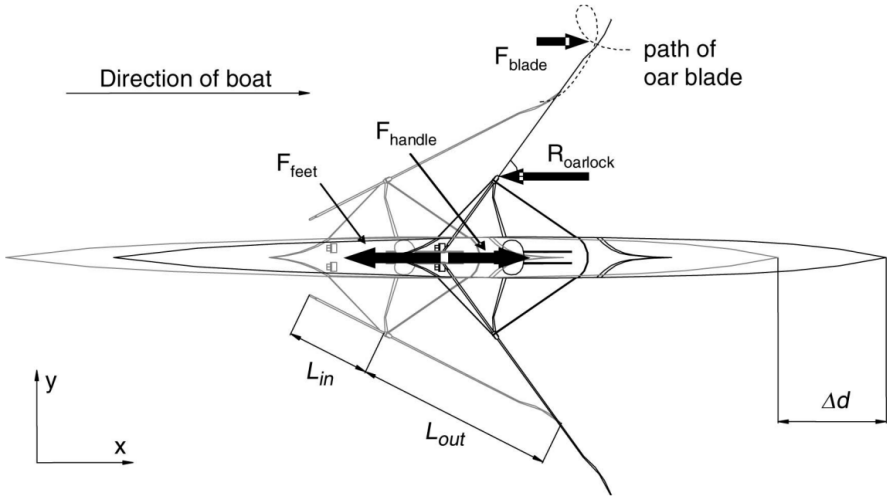

Figure 1.4: The path of the center of the blade relative to the boat, indicated by the dashed lines. Illustration from Caplan and T. N. Gardner (2007).

1.3.2 Blade forces

The movement of the blades relative to the shell is induced by torque generated from the oar handles by the rower. The forces acting on the blade are decomposed to drag F_D, and lift F_L (and can also be further decomposed, see Figure 1.5). Drag forces act tangentially to the blade's movement and lift forces act perpendicular to the movement. Experimental measurements by Grift, Tummers and Westerweel (2021) show that during the beginning stages of the drive, the lift force is the dominant propulsive force. Throughout the stroke, the lift force decreases before a sharp increase occurs towards the finish. The drag force increases throughout the drive and peaks right before the oar is perpendicular to the shell. Similar to the lift force, the drag decreases towards the end of the cycle, with a sharp increase occurring at the finish. The measurements by Grift, Tummers and Westerweel (2021) found drag to contribute to approximately 60 % of the propulsion while the remaining 40 % of the contribution coming from lift. It is therefore necessary to consider both components for propulsive analysis.

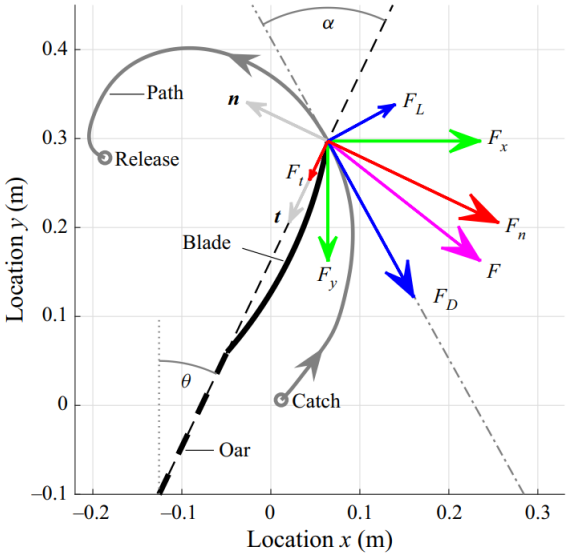

Figure 1.5: Forces acting on the blade, decomposed to lift and drag forces (F_L and F_D), propulsive and non-propulsive forces (F_x and F_y) and normal and tangential forces relative to the blade geometry (F_n and F_t). Illustration from Grift, Tummers and Westerweel (2021).

The forces F_D and F_L are defined as follows:

$$F_D = \frac{1}{2}\rho u^2 C_D A \tag{1.1}$$

$$F_L = \frac{1}{2}\rho u^2 C_L A \tag{1.2}$$

where A is the oar blade surface area, u is velocity for the incoming flow, C_D and C_L are the drag and lift coefficients, respectively, and ρ is the water density.

1.4 Blade geometry

The geometry of the oar blade has changed throughout the history of competitive rowing. A blade geometry called the Macon blade was the standard in high level competitions until 1991 when the blade manufacturer Concept2 introduced the "Big blade". The major difference between these blades is the bigger surface area of the Big blades. Another difference is the shape itself; Macon blade is rounder and symmetrical along the oar shaft, Big blade is more rectangular and not symmetrical along the oar shaft. Both of these blades also have a slight curvature inwards (somewhat similar to a spoon). An illustration of the Big blade and the macon blade is seen in Figure 1.6. There are other smaller changes to the blades done in later years, such as the amount of curvature and slight frontal shape modifications. There has been several studies and papers of the shape of the blade over the recent years. One paper by Caplan and T. N. Gardner (2007) have compared the lift and drag coefficients for Macon and Big blade in a quasi-static steady state experimental investigation for different angles of attack and found the differences between C_L and C_D for the different shapes to depend on angles of attack, where significant higher drag was found for the Big blade at 90° angles of attack.

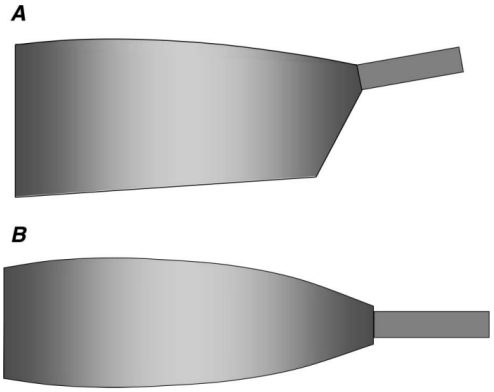

Figure 1.6: Frontal views of the Big blade (A) and the Macon blade (B). Illustration from Caplan and Gardner (2007).

A CFD model by Coppel et al. (2010) with the same quasi-static approach compared drag and lift for a flat and curved Big blade with the experimental measurements done by Caplan and Gardner. This model was able to reproduce the same general pattern for drag and lift coefficients for different angles of attack, but reported some differences between model and experiments, especially for drag.

An issue with the steady state quasi-static approach, pointed out by Caplan and Gardner, is that the vortices created from the blade movement affects the forces, which their model does not take into account. Therefore, other CFD approaches have been carried out to replicate a more realistic scenarios. For example, Sliasas and Tullis (2009) investigated a non-steady rotational flow on a static blade. A takeaway from this paper, pointed out by the authors, is that the rowing stroke includes rotation, translation and surface effects. It is

therefore argued that an accurate numerical simulation of the rowing stroke is difficult.

1.5 Propulsion in swimming

Propulsion in swimming is created by the hands pushed through the water moving the swimmer forward. Comparing it with rowing, the hands of the swimmer plays the same functional role as the oar blade. As swimming is a very popular and developed sport, high interest lies in how to increase propulsive efficiency.

1.5.1 Finger spacing

An important question for propulsive efficiency is weather or not the swimmer should keep his/her fingers spread or closed throughout the swimming motion. Developments in CFD has allowed this issue to be studied more extensively in recent years. Lorente et al. (2012) studied finger spacing using a two dimensional CFD model of multiple cylinders with different spacing between the cylinders for drag force comparison, where the cylinders represented human fingers. Both a steady and transient flow field case were tested. The findings of this study suggest that spacing between the fingers increases the drag force on the swimmers hands compared to closing the fingers for both the transient and steady state case. However, with the same 2D cylinder numerical approach, Darázs and Paál (2016) found drag to be largest with no distance between the cylinders, i.e no finger spacing with a steady state free flow.

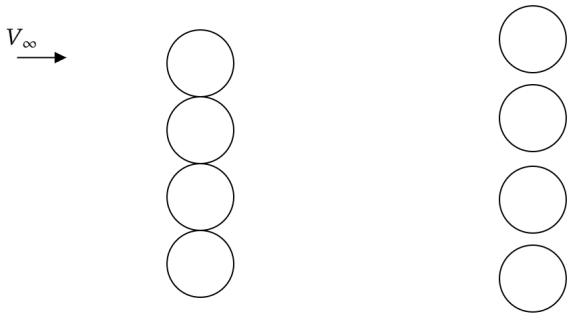

Figure 1.7: A commonly used CFD approach for finger spacing analysis. Flow past 2D cylinders with and without spacing between. Here, V_∞ denotes the free stream fluid velocity.

A limitation of the 2D approach is that the simulations do not capture the three dimensional flow and pressure characteristics. Three dimensional hand models have therefore been tested both experimentally and numerically. Most findings in these studies support the finger spacing hypothesis (Houwelingen et al. 2017; Marinho et al. 2010; Minetti, Machtsiras and Masters 2009). The reason for increased drag is discussed by Minetti, Machtsiras and Masters (2009), where

it is stated that spacing between the fingers creates water jets that counteract vortex formation on the dorsal side of the hand. Sidelnik and Young (2006), who also found finger spread to increase drag, argued that the increased area the fingers span contributes to the increase in drag. There currently seems to be good evidence for spacing the fingers while swimming to increase propulsive efficiency.

A summary of the studies reviewed is found in Table 1.1.

Study	Model	Method	Findings
Lorente et al. (2012)	2D cylinders	Transient and steady state flow (CFD)	Some distance between fingers increases drag force on hands for steady state and transient flow
Darázs and Paál (2016)	2D cylinders	Steady stade (CFD)	No distance between fingers generated the largest drag force
Minetti, Machtsiras and Masters (2009)	3D hand model	CFD	Three different cases investigated (no spacing, medium spacing, large spacing). Largest drag force on medium spaced case
Marinho et al. (2010)	3D hand model	Steady state (CFD)	Spreading the fingers gave higher drag than no spread
Houwelingen et al. (2017)	3D hand model	Experimental and CFD (LES)	Spreading the fingers gave the highest drag both experimentally and numerically
Sidelnik and Young (2006)	Hand model submerged and rotated through water tank	Experimental	Spreading the fingers increased drag force

Table 1.1: Summary of reviewed studies done on finger spacing.

1.6 Outline

Combining studies from rowing and swimming propulsion sets up the basis for the objective of this thesis. The rest of the thesis is organised as follows:

Chapter 2 : The theoretical background will be outlined. This includes the relevant mathematical and numerical topics for this thesis.

Chapter 3 The fluid domain, meshing methodology and some additional numerical treatments will be outlined and discussed.

Chapter 4 The results and will be presented with comments on some observations

Chapter 5 A discussion of the results will be provided, limitations of the study will be discussed and a conclusion will be formed.

CHAPTER 2

Theoretical background

2.1 Governing equations

Modern fluid dynamics is based on the work done by Claude-Louis Navier and George Stokes. Their work led to the Navier-Stokes equations, a set of non-linear partial differential equations, which are derived via mass conservation and by applying Newtons second law to fluid motions. Decomposed for each spatial direction and expressed in Cartesian coordinates, they take the form:

$$\frac{\partial \rho}{\partial t} + \frac{\partial(\rho u)}{\partial x} + \frac{\partial(\rho v)}{\partial y} + \frac{\partial(\rho w)}{\partial z} = 0 \tag{2.1}$$

$$x: \quad \frac{\partial(\rho u)}{\partial t} + u\frac{\partial(\rho u)}{\partial x} + v\frac{\partial(\rho u)}{\partial y} + w\frac{\partial(\rho u)}{\partial z} = -\frac{\partial p}{\partial x} + \mu\left(\frac{\partial^2 u}{\partial x^2} + \frac{\partial^2 u}{\partial y^2} + \frac{\partial^2 u}{\partial z^2}\right) + \rho g_x \tag{2.2}$$

$$y: \quad \frac{\partial(\rho v)}{\partial t} + u\frac{\partial(\rho v)}{\partial x} + v\frac{\partial(\rho v)}{\partial y} + w\frac{\partial(\rho v)}{\partial z} = -\frac{\partial p}{\partial y} + \mu\left(\frac{\partial^2 v}{\partial x^2} + \frac{\partial^2 v}{\partial y^2} + \frac{\partial^2 v}{\partial z^2}\right) + \rho g_y \tag{2.3}$$

$$z: \quad \frac{\partial(\rho w)}{\partial t} + u\frac{\partial(\rho w)}{\partial x} + v\frac{\partial(\rho w)}{\partial y} + w\frac{\partial(\rho w)}{\partial z} = -\frac{\partial p}{\partial z} + \mu\left(\frac{\partial^2 w}{\partial x^2} + \frac{\partial^2 w}{\partial y^2} + \frac{\partial^2 w}{\partial z^2}\right) + \rho g_z \tag{2.4}$$

They can also be written on the more compact form using tensor notation:

$$\frac{\partial \rho}{\partial t} + \frac{\partial u_i}{\partial x_i} = 0 \tag{2.5}$$

$$\frac{\partial(\rho u_i)}{\partial t} + \frac{\partial(\rho u_i u_j)}{\partial x_j} = -\frac{\partial p}{\partial x_i} + \mu\frac{\partial^2 u_i}{\partial x_j \partial x_j} + \rho g_i \tag{2.6}$$

Here, u_i is the velocity vector, ρ is the fluid density, p is pressure, μ is the fluid's viscosity and g_i is gravity forces. The form of the Navier-Stokes equations written here are limited to Newtonian fluids, fluids where the viscous stresses are linearly proportional to the local strain rate, which is the case in this study. Physically, equation (2.5) describes mass conservation and equation (2.6) describes momentum conservation.

2.2 Turbulence

Fluid flow can be separated in two categories: laminar and turbulent flow. Whether a flow is turbulent or laminar can be determined by the non-dimensional Reynolds number, defined as:

$$Re = \frac{\rho u L}{\mu}. \tag{2.7}$$

Here L is a characteristic linear dimension (can typically be the length of an object), and u is the characteristic fluid velocity. The Reynolds number quantifies the ratio between inertial and viscous forces. In turbulent flow, the Reynolds number is large, meaning inertial forces dominate viscous forces. There is no exact value for where a particular flow is turbulent, translation from laminar to turbulent flow depends on characteristics of the particular fluid problem. As an example, Narasimhamurthy and Andersson (2009) found, using CFD, that the flow regime of the wake region for normal flow over a flat plate inherent turbulent characteristics at $Re = 750$. For other flow occurrences, a higher Reynolds number will usually be associated with turbulent characteristics (White and Majdalani 2006).

2.2.1 Physical description of turbulence

A precise definition of turbulence does not exist, and turbulent flow is often rather described by its physical characteristics. In White and Majdalani (2006) the following characteristics were listed:

1. *Fluctuations* in velocity, pressure and potentially temperature when there is heat transfer. Fluctuations happens in all three spatial directions
2. *Eddies* which intermingles and fill the shear layer. Eddy size varies continuously from the shear layer-thickness δ down to the Kolmogorov length scale, $L = (\frac{\nu^3 \delta}{U^3})^{\frac{1}{4}}$ *
3. *Random* variations in fluid properties, where each property has a specific continuous energy spectra which drops of to zero at high wave numbers (small eddy size)
4. *Self-sustaining* motion. Once triggered, turbulent flow can maintain itself by replacing eddies lost to viscous dissipation
5. *Mixing* which is much stronger that that due to laminar (molecular) action. The turbulent eddies actively move about all three dimension and cause rapids diffusion of mass, momentum and energy.

*ν here is the kinematic viscosity of the fluid, defined: $\nu = \frac{\mu}{\rho}$

2.3 Turbulence modeling

The Navier-stokes equations are applicable for laminar and turbulent flow. However, for turbulence, all the pressure and velocity terms varies in time due to the fluctuations (Yusuf et al. 2020). Due to the inherent irregularity of turbulence, different modeling approaches has evolved over the years to gain insight of flow and pressure patterns. One set of models used are the RANS models, which is based upon the Reynolds averaged Navier-stokes (RANS) equations proposed in Reynolds (1895). The equations are obtained using Reynolds decomposition, where velocity and pressure is split up to an average part $\bar{u}$, $\bar{p}$ and a fluctuating part u', p' in the following way:

$$u_i = \bar{u_i} + u_i' \tag{2.8}$$

$$p = \bar{p} + p' \tag{2.9}$$

By inserting (2.8) and (2.9) into (2.5) and (2.6), one can obtain

$$\frac{\partial(\rho\bar{u_i})}{\partial x_i} = 0 \tag{2.10}$$

$$\frac{\partial(\rho\bar{u_i})}{\partial t} + \frac{\partial(\rho\bar{u_i}\bar{u_j})}{\partial x_j} = -\frac{\partial\bar{p}}{\partial x_i} + \mu\frac{\partial^2\bar{u_i}}{\partial x_j\partial x_j} - \frac{\partial}{\partial x_j}(\rho\overline{u_i'u_j'}) + \rho g_i \tag{2.11}$$

The only difference found between these terms and the regular Navier-Stokes equations is the term $\frac{\partial}{\partial x_j}(\rho\overline{u_i'u_j'})$. $(\overline{u_i'u_j'})$ is the *Reynolds stress term*, giving rise to the *Reynolds stress tensor*, a matrix containing six unknowns. This makes the system (2.10), (2.11) unclosed. The Reynolds stress tensor is expressed as follows:

$$\overline{u_i'u_j'} = \begin{bmatrix} \overline{u'^2} & \overline{u'v'} & \overline{w'u'} \\ \overline{v'u'} & \overline{v'^2} & \overline{v'w'} \\ \overline{u'w'} & \overline{v'w'} & \overline{w'^2} \end{bmatrix} \tag{2.12}$$

The diagonal terms are referred to as normal stresses while the the symmetric upper and lower terms are referred to as shear stresses. The different RANS turbulence models have different ways of dealing with this term. Some of these, listed in Alfonsi (2009), includes the *zero-equation models*, the *one-equation models* and the *two-equation models*. The key takeaway with the RANS models is that they resolve all the turbulent lenght scales by modeling. In contrast, another method called the DNS (Direct numerical simulation) model resolves every turbulent lenght scale directly. An in between approach between these models are the LES models (Large eddy simulation) where large eddies within the flow are resolved, and smaller ones are modeled. These approaches are more accurate but comes at significantly greater computational cost. Thus the different RANS models are considered more practical for a many engineering problems (C. J. Chen 1997). The model used in this thesis is within the two-equation models and will be further discussed in section 2.2.3.

2.3.1 The $k-\varepsilon$ model

A common two-equations model used is the standard $k-\varepsilon$ model, introduced by Launder and D. Spalding (1974). The reason for the name two-equation models is that it solves two equations, additional to (2.10) (2.11), that characterises turbulence: the turbulent kinetic energy k and the turbulent dissipation rate ε (dimensions $\frac{m^2}{s^3}$). Turbulent kinetic energy is defined by the mean fluctuations of velocity in each spatial direction:

$$k = \frac{1}{2}(\overline{u_i' u_i'}) \tag{2.13}$$

and ε is defined from the product of the averaged fluctuating components of the *rate of deformation tensor* s_{ij}:

$$\varepsilon = 2v\overline{s_{ij}' s_{ij}'}. \tag{2.14}$$

A more thorough derivation and description of every component here and onward in this section can be found in Versteeg and Malalasekera (2007). Using Boussinesq hypothesis (Boussinesq 1877), the Reynolds stress term can be expressed as follows:

$$-\rho\overline{u_i' u_j'} = \mu_t \left(\frac{\partial \bar{u}_i}{\partial x_j} + \frac{\partial \bar{u}_j}{\partial x_i} \right) - \frac{2}{3}\rho k \delta_{ij}. \tag{2.15}$$

Here, δ_{ij} is the Kronecker-delta, being 1 if $i = j$ and 0 otherwise. The calculation of k and ε are used to evaluate the *eddy viscosity* μ_t expressed in the equation. The transport equation solved for the kinetic energy and the dissipation rate take the form:

$$\frac{\partial(\rho k)}{\partial t} + \frac{\partial(\rho k \bar{u_j})}{\partial x_j} = \frac{\partial}{\partial x_j}\left[\frac{\mu_t}{\sigma_k} \frac{\partial k}{\partial x_j} \right] + 2\mu_t \bar{s}_{ij} \bar{s}_{ij} - \rho\varepsilon \tag{2.16}$$

$$\frac{\partial(\rho \varepsilon)}{\partial t} + \frac{\partial(\rho \varepsilon \bar{u_j})}{\partial x_j} = \frac{\partial}{\partial x_j}\left[\frac{\mu_t}{\sigma_\varepsilon} \frac{\partial \varepsilon}{\partial x_j} \right] + C_{1\varepsilon}\frac{\varepsilon}{k} 2\mu_t \bar{s}_{ij} \bar{s}_{ij} - C_{2\varepsilon}\rho\frac{\varepsilon^2}{k} \tag{2.17}$$

where $\bar{s}_{ij}$ expresses the mean component of the rate of deformation tensor. The equation for μ_t takes the form:

$$\mu_t = \rho C_\mu \frac{k^2}{\varepsilon}. \tag{2.18}$$

The parameters σ_k, σ_ε, $C_{1\varepsilon}$, $C_{2\varepsilon}$ and C_μ in equations (2.16)-(2.18) are model constants. Solving (2.18) from (2.16) and (2.17) allows us to close the system and evaluate the RANS equations (2.10) and (2.11).

The $k-\varepsilon$ model has been widely applied and is known to produce good results for many turbulent flow problems. However, it is also known to perform poorly for flow separation around bluff bodies (Versteeg and Malalasekera 2007). Due to this, the $k-\varepsilon$ model is not the most appropriate for the rowing blade simulations.

2.3.2 The $k-\omega$ model

The most prominent alternative to $k-\varepsilon$ within the two equations-models is the $k-\omega$ model, proposed D. C. Wilcox (1988). It uses *turbulence frequency* $\omega = \frac{k}{\varepsilon}$ (dimension s^{-1}) in the second transport equation. The transport equations to solve becomes:

$$\frac{\partial(\rho k)}{\partial t} + \frac{\partial(\rho k \bar{u_j})}{\partial x_j} = \frac{\partial}{\partial x_j}\left[\left(\mu + \frac{\mu_t}{\sigma_k}\right)\frac{\partial k}{\partial x_j}\right] + P_k - \beta^* \rho k \omega \tag{2.19}$$

$$\begin{aligned}\frac{\partial(\rho\omega)}{\partial t} + \frac{\partial(\rho\omega \bar{u_j})}{\partial x_j} =& \frac{\partial}{\partial x_j}\left[\left(\mu + \frac{\mu_t}{\sigma_\omega}\right)\frac{\partial \omega}{\partial x_j}\right] \\ &+ \gamma_1\left(2\rho\bar{s}_{ij}\bar{s}_{ij} - \frac{2}{3}\rho\omega\frac{\partial \bar{u_i}}{\partial x_j}\delta_{ij}\right) - \beta_1\rho\omega^2\end{aligned} \tag{2.20}$$

with the eddy viscosity given by

$$\mu_t = \frac{\rho k}{\omega}. \tag{2.21}$$

The term P_k is given by

$$P_k = \left(2\mu_t\bar{s}_{ij}\bar{s}_{ij} - \frac{2}{3}\rho k\frac{\partial \bar{u_i}}{\partial x_j}\delta_{ij}\right) \tag{2.22}$$

and the parameters σ_k, σ_ω, γ_1,, β_1 and β^* are model constants. As with the $k-\varepsilon$ model, evaluating (2.21) from (2.19) and (2.20) allows us to close the system using (2.15). An important advantage with the $k-\omega$ model is that it predicts flow near walls with adverse pressure gradients more accurately (D. Wilcox 1991). The disadvantage it has compared to $k-\varepsilon$ is that it is sensitive to small changes in the free stream inlet conditions (Kok 2000).

2.3.3 The $k-\omega$ SST model

The $k-\omega$ SST model, where SST stands for *shear stress transport*, is a hybrid between the $k-\varepsilon$ and the $k-\omega$ model, proposed by Menter (1994). It utilizes the advantages of $k-\omega$ in the near wall with adverse pressure gradients, but switches to the $k-\varepsilon$ in the fully turbulent regions to circumvent the issues with free stream sensitivity discussed in the previous section. The only changes done to the transport equations compared to the $k-\omega$ models is the substitution $\varepsilon = k\omega$ in to the ε-equation (2.17). This leads to the equation:

$$\begin{aligned}&\frac{\partial(\rho\omega)}{\partial t} + \frac{\partial(\rho\omega \bar{u_j})}{\partial x_j} = \frac{\partial}{\partial x_j}\left[\left(\mu + \frac{\mu_t}{\sigma_{\omega,1}}\right)\frac{\partial \omega}{\partial x_j}\right] \\ &+ \gamma_2\left(2\rho\bar{s}_{ij}\bar{s}_{ij} - \frac{2}{3}\rho\omega\frac{\partial \bar{u_i}}{\partial x_j}\delta_{ij}\right) - \beta_2\rho\omega^2 + 2\frac{\rho}{\sigma_{\omega,2}\omega}\frac{\partial k}{\partial x_k}\frac{\partial \omega}{\partial x_k}.\end{aligned} \tag{2.23}$$

The difference between this equation and (2.20) is the last term and some revised model constants. The SST model uses blending functions in order to ensure a smooth transition between the regions of the flow using $k-\varepsilon$ and the regions using $k-\omega$. It also uses limiters, i.e setting a reasonable bound on some of the turbulent properties, mainly k and μ_t. This inhibits the build up of turbulent kinetic energy production in stagnation regions for k, and keeps the eddy viscosity μ_t of getting too large, improving performance in wake regions.

The $k-\omega$ SST model was considered the most suitable for the rowing blade case due to it's performance for flow separation and adverse pressure gradients (Menter, Kuntz and Langtry 2003), which is important for more accurate rowing blade simulations.

2.4 The Finite volume method

In order to evaluate the equations discussed in the previous sections with meaningful results, a *discretization method* must be applied. The purpose of a discretization method is to split up a domain into a finite amount nodes ordered in some sequential structure called a mesh. The finite volume method (FVM), which is used in the simulations for this thesis, is a method for evaluating unknowns in the differential equations discussed earlier at each node of the computational domain using the *divergence theorem*. The divergence theorem is known as:

$$\int_{CV} \frac{\partial a_i}{\partial x_i} = \int_A n_i a_i \mathrm{d}A. \tag{2.24}$$

where CV indicates a *control volume*, A indicates a surface area, dV is a volume element, dA is an area element, a_i represents a continuously differentiable vector and n_i is the vector normal to the surface element dA. Physically, the divergence theorem states that the density within a volume only changes by flow coming into or out of its boundaries, given the absence of matter creation. Using this property allows us express the differential equations we want to solve as a system algebraic equations. Through known techniques from linear algebra can we solve for the unknown quantities (such as velocity, pressure, turbulent kinetic energy etc.) at each node in our domain. As before, a detailed description of how this process works in practise can be found in Versteeg and Malalasekera (2007).

2.5 Chapter summary

In this chapter, relevant mathematical background theory has been briefly outlined and discussed. In the subsequent chapter, case preparation and some numerical considerations to be made will be discussed.

CHAPTER 3

Case preparation

3.1 Simulation set up

The inherent complexity of realistic blade-water interactions in the rowing stroke poses many modeling challenges. Some of these include how to treat the blades effect on the water surface, and how to generate well resolved and realistic dynamic meshes. To study blades with slits with CFD, a simplified scenario of the rowing blade was considered in this study. The approach taken is a static investigation, where the oar blade is held fixed beneath the water surface in moving flow field. For benchmark comparisons, the CFD simulations are set up in the same manner as the experimental study by Caplan and T. N. Gardner (2007). Here, the oar blade is static for different angles of attack α and forces were measured. In the present study, three angles of attack (AOA) included by Caplan and T. N. Gardner (2007) will be tested; 45 AOA, 90 AOA and 115 AOA. An illustration of the quasi static approach used is shown in Figure 3.1. The full fluid domain is illustrated in Figure 3.2

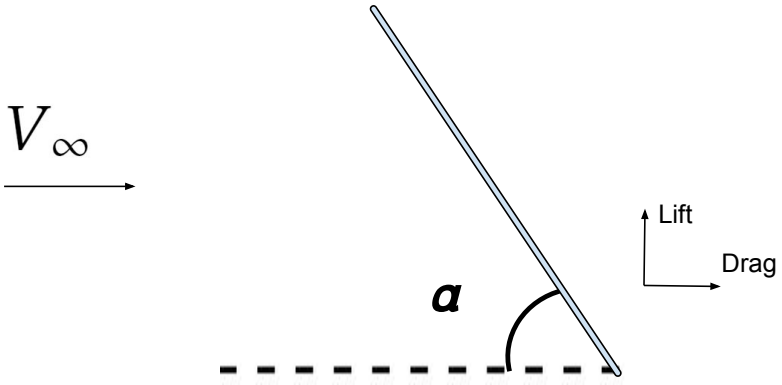

Figure 3.1: View of the static approach for varying angles of attack α between free stream orientation and the blade chord line. V_∞ denotes the free stream fluid velocity.

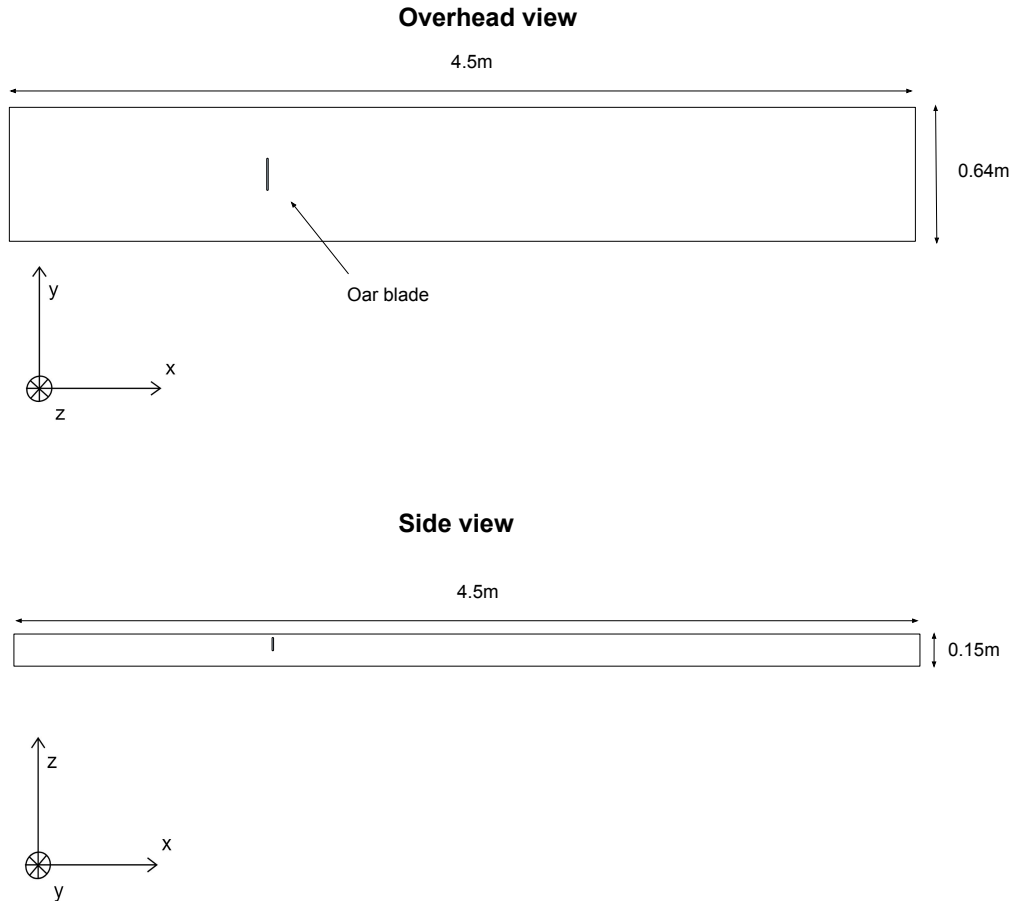

Figure 3.2: The fluid domain. The blade is submerged 5mm beneath the surface and held static with an incoming flow.

There are many different blade slit configurations that can be investigated. In this thesis, two slit modifications were investigated: the slit thickness and the number of slits on the blade. We will measure how drag and lift coefficients vary depending on these parameters. Before details of the geometry and the rest of the preparation are outlined the software used for the simulations will be briefly discussed.

3.2 OpenFOAM

Every simulation in this thesis is done in OpenFOAM (**Open**-source **F**ield **O**peration **A**nd **M**anipulation), a C++ based software package for setting up and executing CFD simulations. It contains a wide range of custom based solvers for different CFD applications. The user sets up a case by modifying solvers, initial physical parameters, and geometrical inputs to fit their desired case.

Boundary conditions, which model to use (i.e k-ϵ, LES), transport properties and which solver to execute is then decided before running a case.

Although OpenFOAM doesn't have a graphical user interface, the code structure often closely resembles the mathematically expressed equations. For example, the equation:

$$\frac{\partial \rho \mathrm{U}}{\partial t} + \nabla \cdot \phi \mathrm{U} - \nabla \cdot \mu \nabla \mathrm{U} = -\nabla p$$

is written by the code:

```
solve
(
    fvm::ddt(rho, U)
  + fvm::div(phi, U)
  - fvm::laplacian(mu, U)
  ==
  - fvm::grad(p)
);
```

This allows for flexibility and easy customization, made possible from the features of object oriented coding OpenFOAM utilizes from C++.

3.2.1 OpenFOAM case set up

OpenFOAM is executed within a root folder that contains a specific file directory structure. A typical directory structure of an OpenFOAM case, here when the k-ω model is used, is illustrated by the figure below.

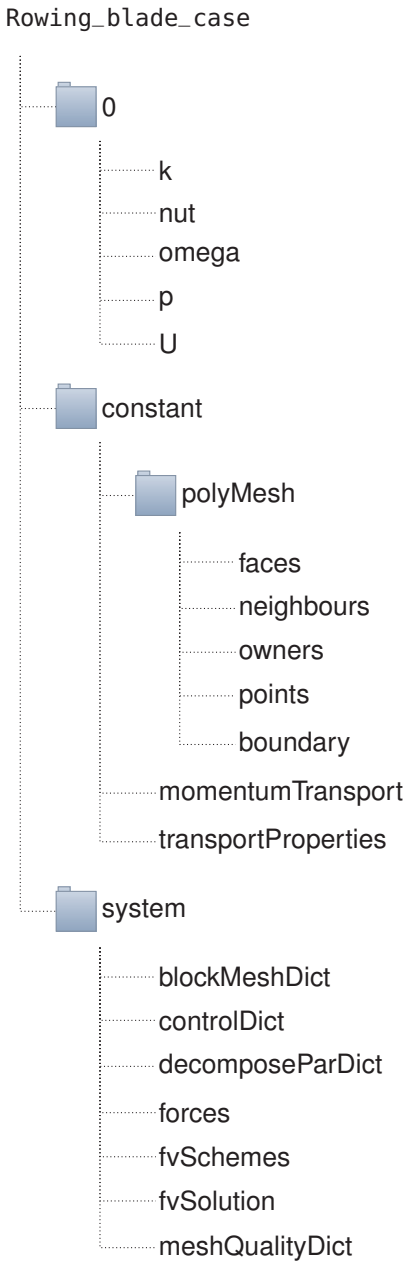

Figure 3.3: Overview of the OpenFOAM® case structure.

The directories 0, constant and system will be present in any OpenFOAM case. The 0 folder contains dictionaries where physical properties of the simulation are determined, the constant folder contains dictionaries with mesh, transport/turbulence and momentum properties, and the system folder contains dictionaries where various parameters for the solution procedure can be adjusted. If the files within the case-folder and it's sub-directories is set up correctly, a simulation can be initiated by writing the preferred solver (here simpleFoam) in the command line from the root folder:

```
[user Rowing_blade_case]$ simpleFoam > log&
```

The > log& addition will write down information about the simulation in a txt-file, and allows for other tasks with the terminal to be done as the simulation runs. The txt-file written out contains information about the residuals, execution time and other features which all can be customized by modifying the `controlDict` inside the system folder.

3.3 Blade geometries

The starting point of the mesh generation procedure was the creation of STL files. An STL file is a file that represents a physical geometry, which can be visualized in a graphics software. This was done in SALOME, a multi-platform open source software containing a lot of engineering purposed features. A flat plate with comparative dimensions to the Big blade was created with rounded out edges (see figure Figure 3.4). The thickness of the blade is 1.8 mm, height and length are 57 mm and 135 mm, respectively. The blade created does not have any curvature like a regular Big blade, but a similar blade was measured in the experimental study by Caplan and T. N. Gardner (2007) so a good comparison of the model can be acquired.

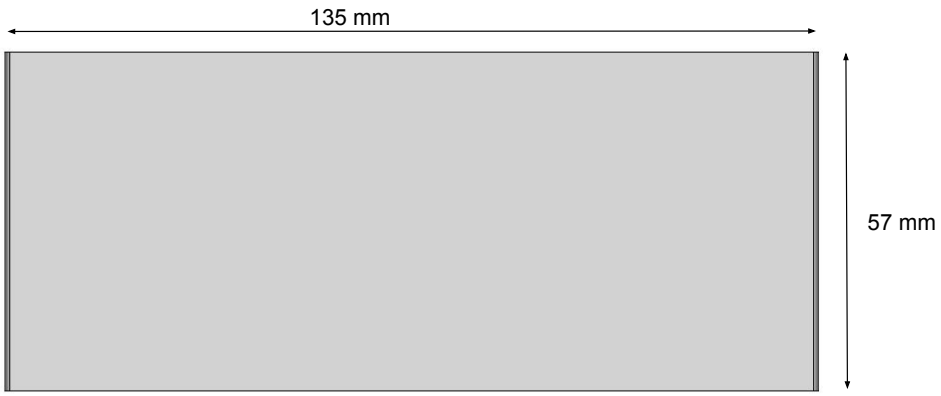

Figure 3.4: Frontal view of the solid flat oar blade created in SALOME. Thickness of the blade is 1.8 mm.

Five different blade configurations were created with similar length, height and thickness for comparison with the regular solid blade.

(a) Large slits.

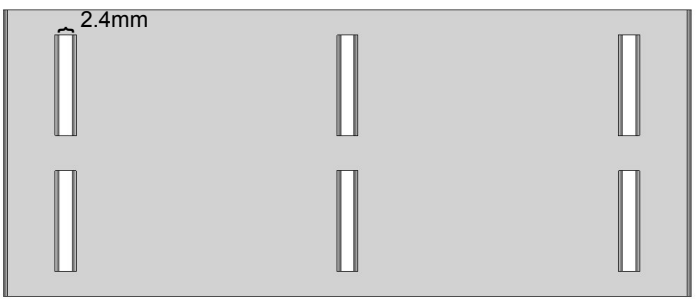

(b) Medium slits.

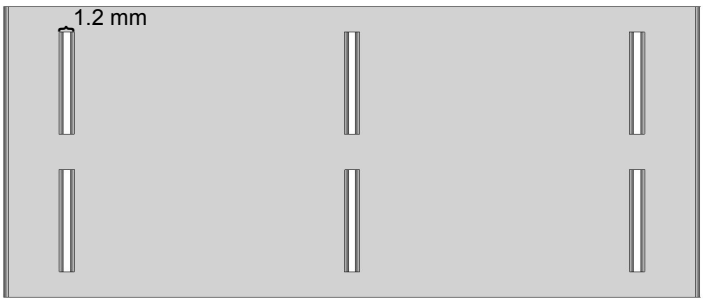

(c) Small slits.

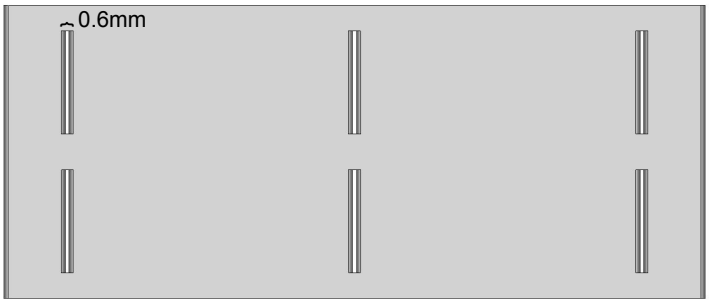

Figure 3.5: The different variations in slit size.

(a) 12 slits.

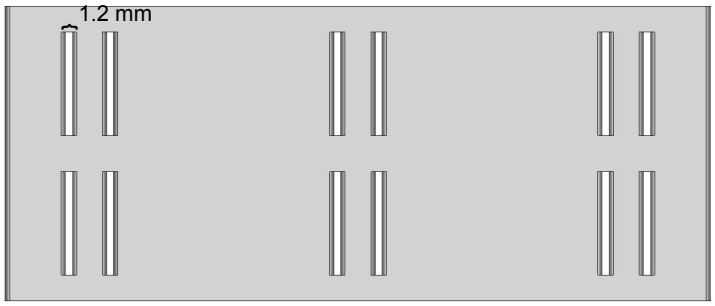

(b) 24 slits.

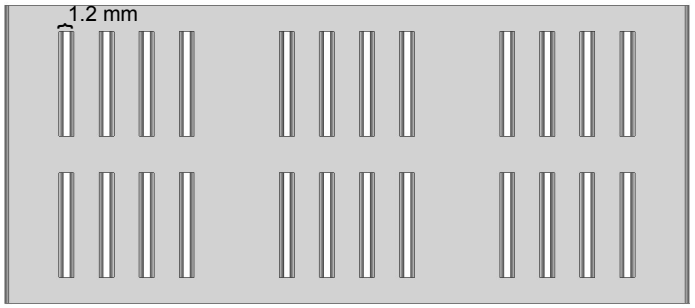

Figure 3.6: The different variations in amount of slits.

3.4 Meshing considerations

In order to gain meaningful results, well performing meshes had to be generated. The mesh quality can have significant effect on the results of the simulations (Oberkampf and Trucano 2002), and there are a well known features of the mesh that need careful consideration. Some of these will be briefly discussed in the next sections.

3.4.1 Non-orthogonality

As discussed in Section 2.4, the finite volume method is used to evaluate physical values for every cell center (or node) in the domain. The standard form of the transport equation for a scalar value ϕ can be expressed in the following way:

$$\underbrace{\frac{\partial \rho\phi}{\partial t}}_{\text{Temporal derivative}} + \underbrace{\frac{\partial(\rho u_i \phi)}{\partial x_i}}_{\text{convection term}} - \underbrace{\frac{\partial^2(\rho\Gamma_\phi\phi)}{\partial x_i \partial x_i}}_{\text{diffusion term}} = \underbrace{S_\phi(\phi)}_{\text{source term}} \tag{3.1}$$

Here, the diffusion term needs values for each cell face after the discretization in order to be evaluated with the FVM as this term utilizes the flux through the faces for the calculations. In the figure below, d_i is the vector between cell centers, S_i is the vector normal to the common face of cell P and its neighbouring cell N.

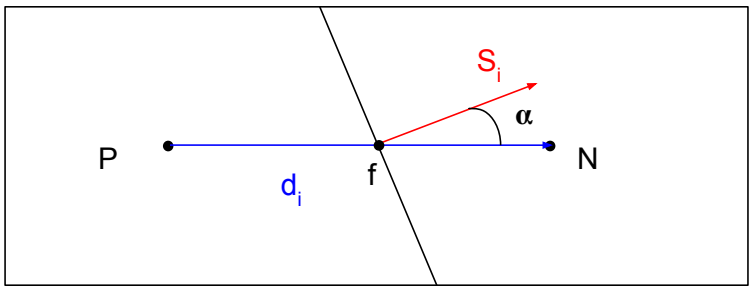

Figure 3.7: Illustration of non-orthogonality between cells. Adopted from Jasak (1996).

The flux term to be evaluated at the face f is $S_i \frac{\partial \phi}{\partial x_j}$. If the vectors S_i and d_i is parallel to each other, this can be done straightforwardly by:

$$S_i \frac{\partial \phi}{\partial x_i} = |S_i| \frac{\phi_N - \phi_P}{|d_i|} \tag{3.2}$$

However, it is not uncommon for angles to be present. To circumvent this a non-orthogonal corrector is implemented. This can be handled by OpenFOAM by turning on "non-orthogonal corrector" in the fvSolution dictonary, but if the angle α proceeds 70 degrees accuracy might suffer or the solution for the flow variables can diverge. Therefore, not exceeding this limit between cells in the mesh is advantageous. A derivation of the flux term expressed and the different non-orthogonal corrector methods can be found in Jasak (1996).

3.4.2 Skewness

Another consideration that stems from the diffusion term in Equation (3.1) is the skewness between cells. Interpolation between ϕ_N and ϕ_P is used to evaluate the face value between these cell centers, but the value is calculated in the point g in the figure below as opposed to the point g_{face}. If the vector m_i is big compared to the vector d_i (between cell centers), the cells are significantly skewed and, as with non-orthogonality, accuracy might be reduced or the solution can diverge.

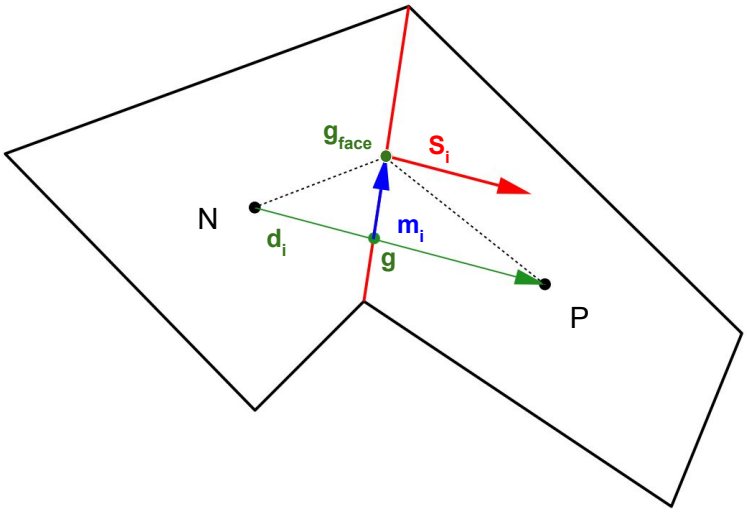

Figure 3.8: Illustration of skewness between cells. Adopted from Jasak (1996).

3.4.3 Aspect ratio

The last mesh feature to be addressed is the aspect ratio. This is the relationship between the longest and shortest side of a cell, illustrated in the figure below. As shown by Almohammadi et al. (2012) big aspect ratios on the cells can lead to less accurate results. Figure 3.9 illustrates to cells with different aspect ratios.

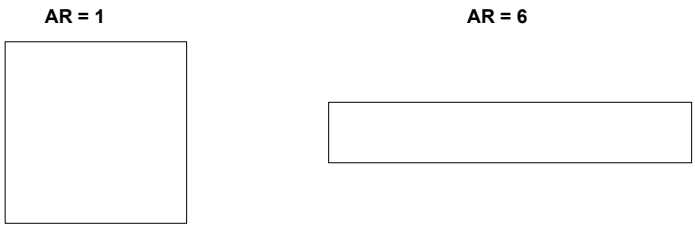

Figure 3.9: Illustration of two 2D cells with different aspect ratios (AR).

This feature does not have any corrector technique like the previously mentioned features, but there exist an upper bound of aspect ratio which should not be exceeded.

3.4.4 CheckMesh

The way the issues mentioned above can be addressed in OpenFOAM is by the checkMesh command. This will give the user feedback on weather or not the mesh quality is deemed usable. This was used during the meshing procedure for mesh quality evaluation. Below is an example of a snippet of the output from one of the meshes used in this thesis:

```
...
Checking geometry...
    Overall domain bounding box (0 0 0) (4.5 0.64 0.15)
    Mesh has 3 geometric (non-empty/wedge) directions (1 1 1)
    Mesh has 3 solution (non-empty) directions (1 1 1)
    Boundary openness (-1.30151e-16 4.86233e-17 -1.89068e-15) OK.
    Max cell openness = 3.27603e-16 OK.
    Max aspect ratio = 14.3861 OK.
    Minimum face area = 6.76491e-09. Maximum face area = 0.00413258.
    Face area magnitudes OK.
    Min volume = 1.33693e-12. Max volume = 0.00019674.  Total volume = 0.431986.
    Cell volumes OK.
    Mesh non-orthogonality Max: 52.9008 average: 3.57316
    Non-orthogonality check OK.
    Face pyramids OK.
    Max skewness = 2.85781 OK.
    Coupled point location match (average 0) OK.

Mesh OK.
```

As seen, different parameters, including the ones mentioned earlier, are addressed. If one of the parameters exceeds some limit deemed problematic a warning will be given and re-meshing is often necessary.

3.5 Mesh performance

For the meshing itself there exists several meshing softwares to choose from, such as SnappyHexMesh, SALOME meshing or cfMesh. After a trial and error process cfMesh was chosen as it seemed to handle the considerations mentioned in Section 3.4 best for this meshing case. An advantage with cfMesh found was the easy addition of inflation layers and refinement regions and how it performed on these tasks. Inflation layers is needed to model the flow close to the wall due to the steep velocity gradients near the wall without the use of wall functions (more on this in Section 3.5). Refinement regions was used in the wake and close to the stagnation point of the blade to capture the flow variations in this region more accurately. Figure 3.10 shows a cross section of one of the meshes used.

(a) Slice of the full mesh, oar blade position indicated.

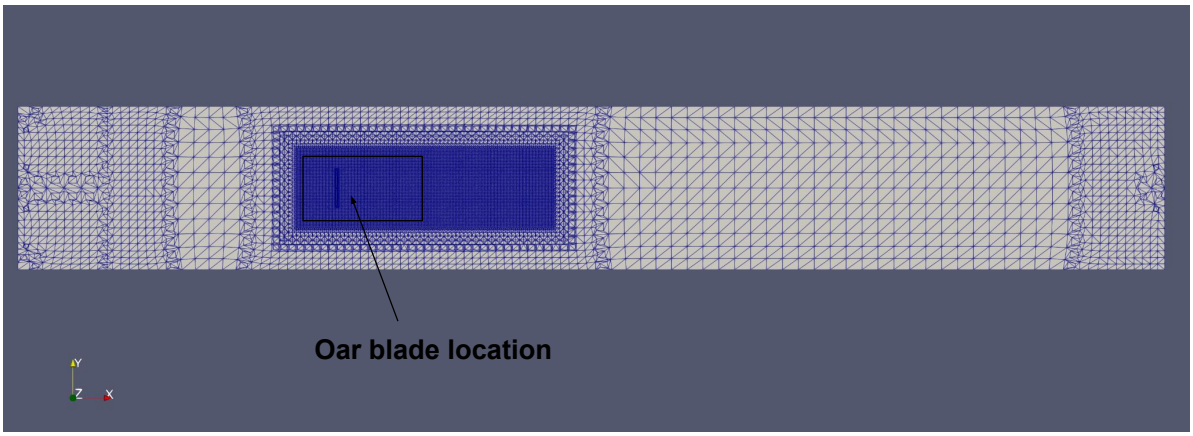

(b) Zoomed in closer to oar position.

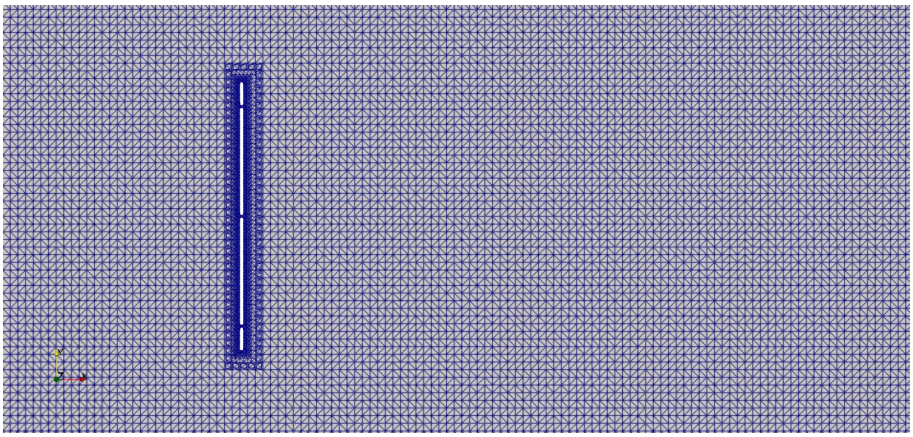

Figure 3.10: The mesh for one of the slit configuration cases constructed in cfMesh. a) Is the full mesh, b) is zoomed close to the blade.

3.5.1 Mesh dependency study

A standard procedure in CFD model evaluation is conducting a mesh dependency study. The goal is to investigate how fine the mesh should be in order for an additional increase in cell amount to have negligible effects on the calculations of interest, mainly drag and lift. For this the regular blade held at 45 °was chosen as it was presumed to have a higher Strouhal Number (J. M. Chen and Fang 1996). This was believed to have greater sensitivity to mesh resolution differences so a good standard could be set.

Three different meshes was simulated for one regular blade and one slit configured blade. Table 3.1 and Table 3.2 summarize the mesh dependency found. The coarse meshes are without a refinement region near the blade and wake region, the medium meshes has some refinement in this region and the fine meshes has high refinement in this region. As can be seen, the differences in C_D and C_L are smaller from medium to fine resolution than from coarse to medium resolution. The fine mesh in this case was seen as a reasonable trade off between accuracy and computational time.

Mesh resolution	Coarse	Medium	Fine
No. of cells	418637	1062750	3182535
C_D	0.891	0.940	0.946
C_L	0.895	0.949	0.958
y^+_{mean}	1.853	0.591	0.278

Table 3.1: Mesh dependency test for a solid blade at 45 °angles of attack.

Mesh resolution	Coarse	Medium	Fine
No. of cells	517809	866812	3166437
C_D	0.887	0.914	0.908
C_L	0.868	0.896	0.892
y^+_{mean}	0.974	0.603	0.282

Table 3.2: Mesh dependency test for a blade with slits at 45 °angles of attack.

Further info on how these coefficients were evaluated will be outlined in Chapter 4.

3.5.2 Wall treatment and y+

Modeling the flow field near the wall with CFD poses some challenges which can be handled with different approaches. To determine how the flow varies depending on its distance to the wall, two well known variables are used; the dimensionless wall distance variable y^+ and the dimensionless velocity u^+. They take the form:

$$y^+ = \frac{yu_\tau}{\nu} \tag{3.3}$$

$$u^+ = \frac{u}{u_\tau} \tag{3.4}$$

where y is the wall distance, u is the velocity and u_τ is the friction velocity, defined by the wall shear stress τ_w and fluid density ρ as:

$$u_\tau = \sqrt{\frac{\tau_w}{\rho}} \tag{3.5}$$

Very close to the wall the fluid is dominated by the viscous effects, and the relationship between y^+ and u^+ is found to be:

$$u^+ = y^+ \quad \text{if} \quad y^+ < 5 \tag{3.6}$$

This region is know as the viscous sub-layer, characterised by steep velocity gradients. In this region, an additional refinement, known as inflation layers is needed in the mesh to resolve rapidly changing fluid properties. If inflation layers is not achieved or deemed to computationally expensive, the use of wall function is an alternative approach. In this thesis, the former approach was chosen as it is generally more accurate if the mesh is sufficiently resolved. The inflation layers generated by cfMesh are shown in Figure 3.11 Determining if the first cell center of the refined region is within the viscous sub-layer can be done in OpenFOAM by the command:

```
[user Rowing_blade_case]$ simpleFoam -postProcess -func yPlus
```

which returns max, mean and average y^+ values for the cell centers near the wall. A rule of thumb is to try, if possible, to have $y^+_{mean} \simeq 1$ in addition to a reasonable bound on y^+_{max}. More on y^+ for CFD simulations can be found in Eça, Pereira and Vaz (2018). In every simulation used in this thesis, $y^+_{mean} < 1$ was ensured using the command above.

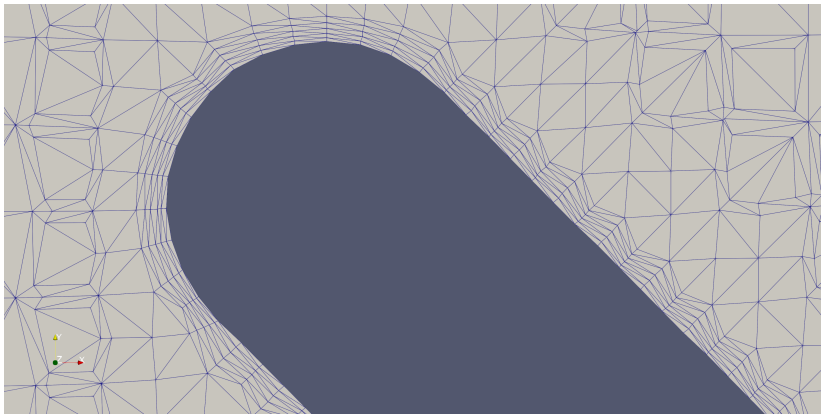

Figure 3.11: Inflation layers close to the blade surface generated by cfMesh. The distance between the straight blade surface lines is 1.8mm (blade thickness).

3.6 Chapter summary

This chapter has outlined how the numerical simulations are prepared and what considerations has been made in this regard. In the following chapter, the boundary conditions used will be outlined and the results for the different blade configurations will be presented and commented.

CHAPTER 4

Results

4.1 Preliminary information

Before discussing boundary conditions and presenting the results, the geometrical details of the blades will be presented and some abbreviations will be introduced. The rowing blades with different slit configurations are categorized by two main parameters: the slit width and the number of slits. The three different width sizes tested are categorized as small slits, medium slits and large slits configuration, with each of these blades containing six slits. In addition, with the medium slits configuration, three different slit number configurations are tested: 6 slits, 12 slits and 24 slits. For convenience, some abbreviations will be introduced. The abbreviations for the size variations will be as following: LS (large slits), MS (medium slits) and SS (small slits). For the amount variations it will be 12S (12 slits) and 24S (24 slits). The case with 6 medium sized slits will remain with its previously defined abbreviation MS. The geometry of the MS variant is shown in Figure 4.1 with additional information about distances between slits, slit sizes and distance from edges.

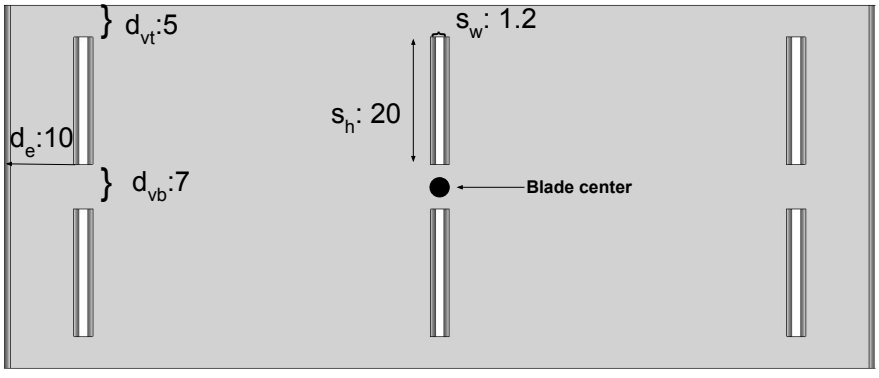

Figure 4.1: Blade geometry for the MS variant with dimensions in mm. d_e denotes distance from edge, d_{vb} denotes vertical distance between slits, d_{vt} denotes vertical distance to the top of the blade, s_h and s_w denotes the slit height and width, respectively. The thickness of the blade is 1.8mm, height and length is 57mm and 135mm, respectively.

The parameters d_{vt}, d_{vb} and s_h are kept constant for every rowing blade

tested. The geometric properties for 24S is shown in Figure 4.2. The rest of the blades were shown in section Section 3.3 (Figure 3.6 and Figure 3.5). Table 4.1 shows information about the geometry of every blade configuration tested.

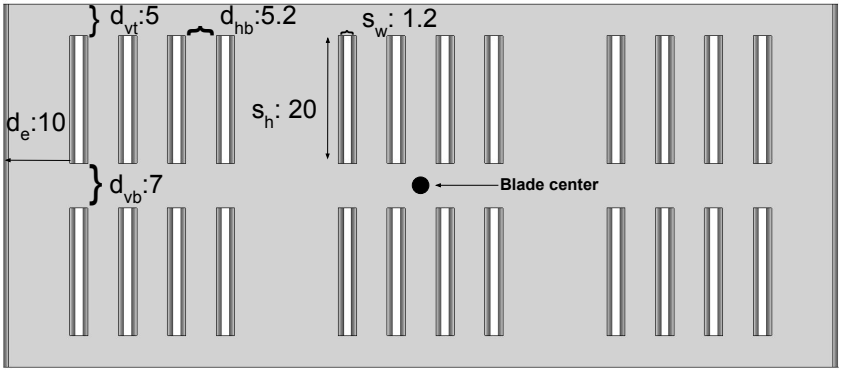

Figure 4.2: Blade geometry for the 24S variant with dimensions in mm. d_e denotes distance from edge, d_{vb} denotes vertical distance between slits, d_{hb} denoted horizontal distance between the local slits, d_{vt} denotes vertical distance to the top of the blade, s_h and s_w denotes the slit height and width, respectively. The thickness of the blade is 1.8mm, height and length is 57mm and 135mm, respectively.

Blade configuration	Regular	SS	MS	LS	12S	24S
s_w (in mm)	0	0.06	1.2	2.4	1.2	1.2
d_e (in mm)	0	10.3	10	9.4	10	10
No of slits	0	6	6	6	12	24
$\frac{\text{slit area}}{\text{blade span area}}$	0	0.0094	0.0187	0.0374	0.0374	0.0749
Projected area (in cm^2)	77.0	76.2	75.5	74.1	74.1	71.2

Table 4.1: Information on the geometry for the different blade configurations.

4.2 Boundary and initial conditions

The boundary conditions used are indicated by Figure 4.3. The inflow velocity for in this case is set at 0.75 ms^{-1}. On the free surface (top of the domain), a symmetry plane was used. This is similar to the CFD study by Coppel et al. (2010) where it was argued that this more closely resembles the free surface than a slip condition would. Additionally, it also decreases computational resources and numerical complexity. Turbulent kinetic energy is set by $k = \frac{3}{2}(U_{in}I)^2$ where U_{in} is the inlet velocity ($0.75ms^{-1}$) and the turbulent intensity I is set at 4% which is similar to Coppel et al. (2010). At the oar blade no-slip was ensured, such that $U_i = 0$ at the blade surface. The pressure conditions at the blade is set as zero-Gradient. The simulations were all ran using the SimpleFoam command in OpenFOAM which utilizes a version of the SIMPLE algorithm (Patankar and D. B. Spalding 1983).

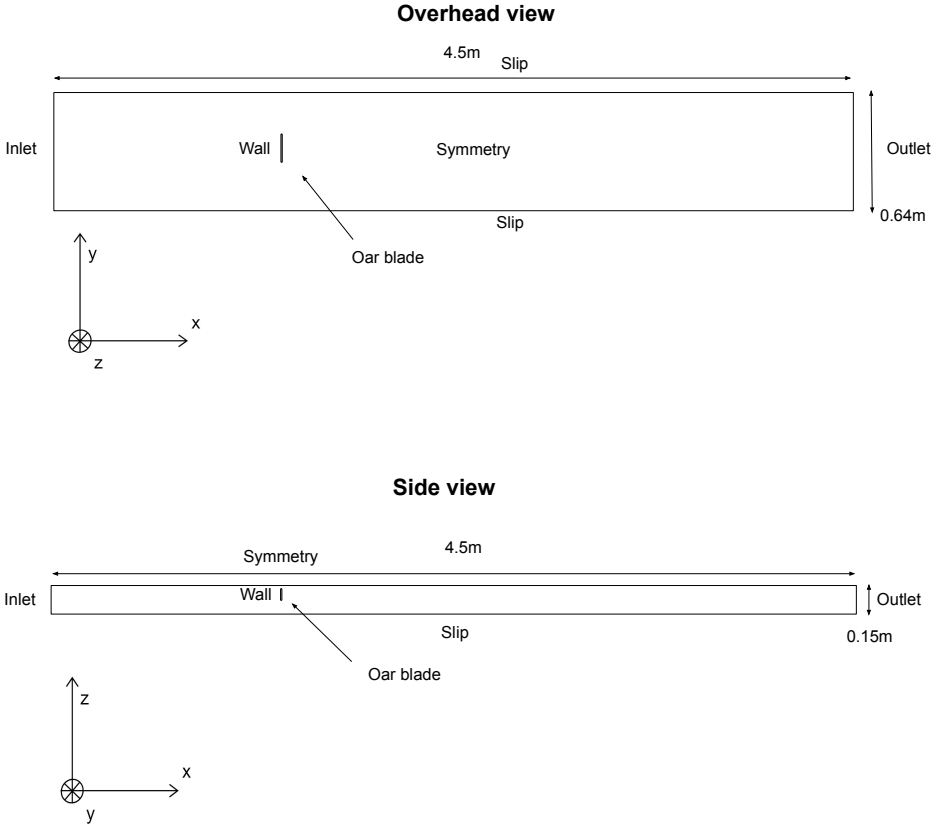

Figure 4.3: Boundary conditions for the computational domain. The "wall" text next to the oar blade indicates a no-slip velocity and zero-Gradient pressure condition. Blade is submerged 5 mm below the surface.

4.3 Model reference

The model accuracy for the regular solid blades was measured by how the drag and lift coefficient compared to the experimental study by Caplan and T. N. Gardner (2007). Similarly to this study the drag and lift coefficients are calculated by:

$$C_D = \frac{2F_D}{\rho u^2 A} \tag{4.1}$$

$$C_L = \frac{2F_L}{\rho u^2 A} \tag{4.2}$$

where F_D is the drag force, F_L is the lift force, ρ is the fluid density, u is the fluid velocity and A is the projected area of the blade. The forces F_D and F_L are calculated by including the #forces function in `controlDict` (shown in Section 3.2: Figure 3.3).

The results for the drag and lift coefficient for the solid blade is found in Figure 4.4 and Figure 4.5. The general trend matches well where drag peaks at 90 AOA while the lift drops to 0 for this angle. We see some underpredictions of the coefficients, most notably at 45 AOA with a 27% decrease in the lift coefficient and a 26 % decrease in drag coefficient. The best prediction was found for at 115 AOA for the lift coefficient with a 13 % decrease in the lift coefficients absolute value.

The relative differences between the current CFD model and the experiment are presented in Table 4.2 and Table 4.3.

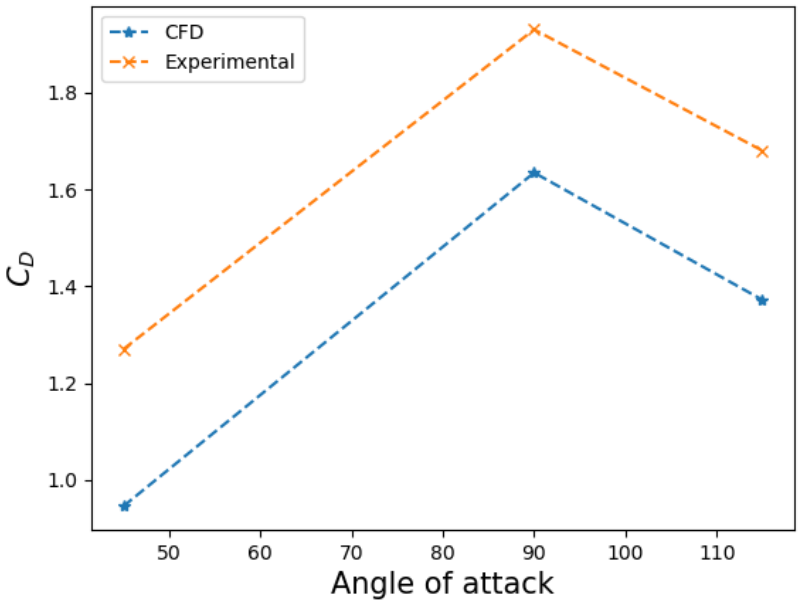

Figure 4.4: Drag coefficient for different angles of attack. Experiments by Caplan and T. N. Gardner (2007) vs CFD in this study.

Angle	C_D CFD	C_D Experimental	Relative difference
45°	0.946	1.270	25.6%
90°	1.646	1.930	15.2%
115°	1.372	1.680	18.3%

Table 4.2: The relative differences in the drag coefficient between experimental values from Caplan and T. N. Gardner (2007) and the CFD study conducted.

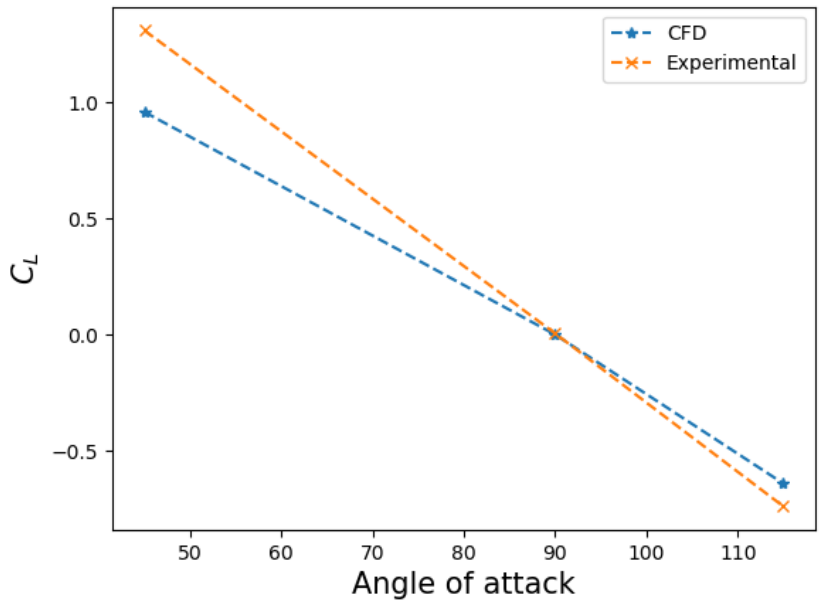

Figure 4.5: Lift coefficients for different angles of attack. Experiments by Caplan and T. N. Gardner (2007) vs CFD in this study.

Angle	C_L CFD	C_L Experimental	Relative difference
45°	0.958	1.310	26.8%
115°	-0.641	-0.740	13.4%

Table 4.3: The relative differences in the lift coefficients between experimental values from Caplan and T. N. Gardner (2007) and the CFD study conducted. The lift values for 90 angles of attack are very small for both cases so they are neglected.

An interesting observation found in Figure 4.4 is how the CFD calculations closely resembles a shift in the curve. This was investigated further by looking into calculation methods in the current CFD study to check if some systematic calculation differences occurred (e.g checking projected area calculations and other constant parameters). As none could be found an additional case with 20 angle of attack was tested to see if this phenomena was consistent for all angles. In this case the CFD calculations got a higher drag coefficient ($C_D = 0.250$ for experimental and $C_D = 0.289$ for CFD). The reason for the consistency in absolute differences between the particular angles in this study remains unknown.

4.4 45 AOA

The drag coefficient for different blade configurations for 45 AOA is shown in Figure 4.6. The drag is maximized for the regular blade (i.e. without slits) reaching approximately 0.94. The drag coefficient decrease nearly linearly

between each configuration and the drag coefficient for a blade with 6 large slits was found to be 0.91. The blade with the most open area (24S) obtained the lowest drag coefficient of approximately 0.88. Thus, a total decrease of around 7% in drag was seen in the 45 AOA case. The lift coefficients, shown in Figure 4.7 revealed substantial decrease with increasing open area. The maximal lift coefficient was obtained with the regular blade, reaching a value of approximately 0.96. The lowest lift was obtained with the 24S configuration with a lift coefficient of approximately 0.77. The decrease in lift coefficient thus amounted to a reduction of 20 % of the lift. Velocity magnitude for the flow fields for all six cases tested are shown in Figure 4.8.

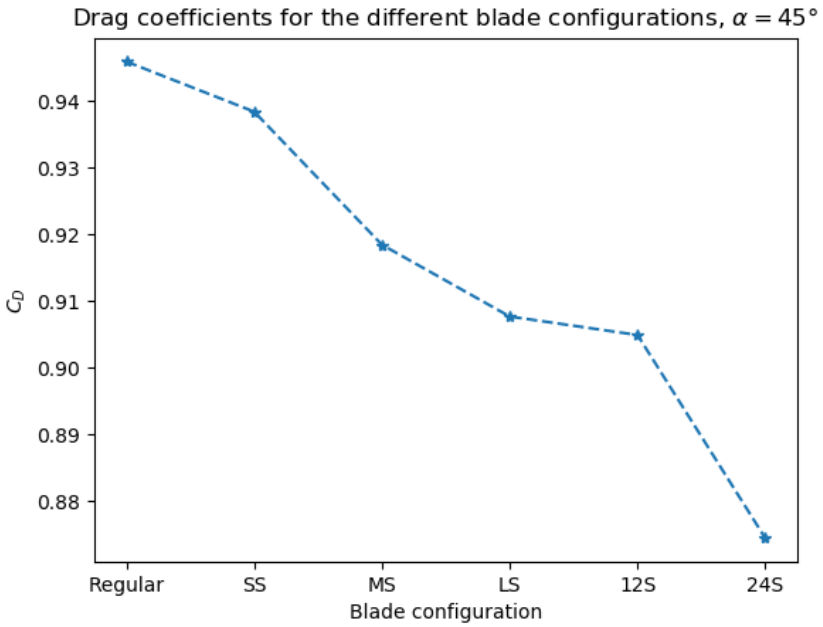

Figure 4.6: Drag coefficients for the different blade configurations held at 45 AOA.

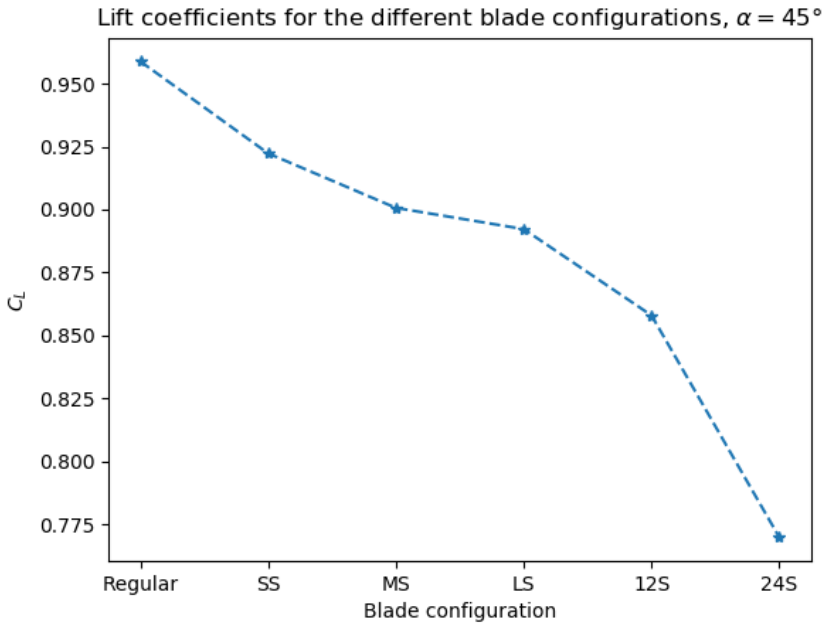

Figure 4.7: Lift coefficients for the different blade configurations held at 45 AOA.

As seen by the figures, the flow penetrates every slit creating small jets in the wake regions. Separation around the leading edge seems somewhat affected by one of the slits for the LS configuration. Otherwise the wake regions do not change substantially between the cases.

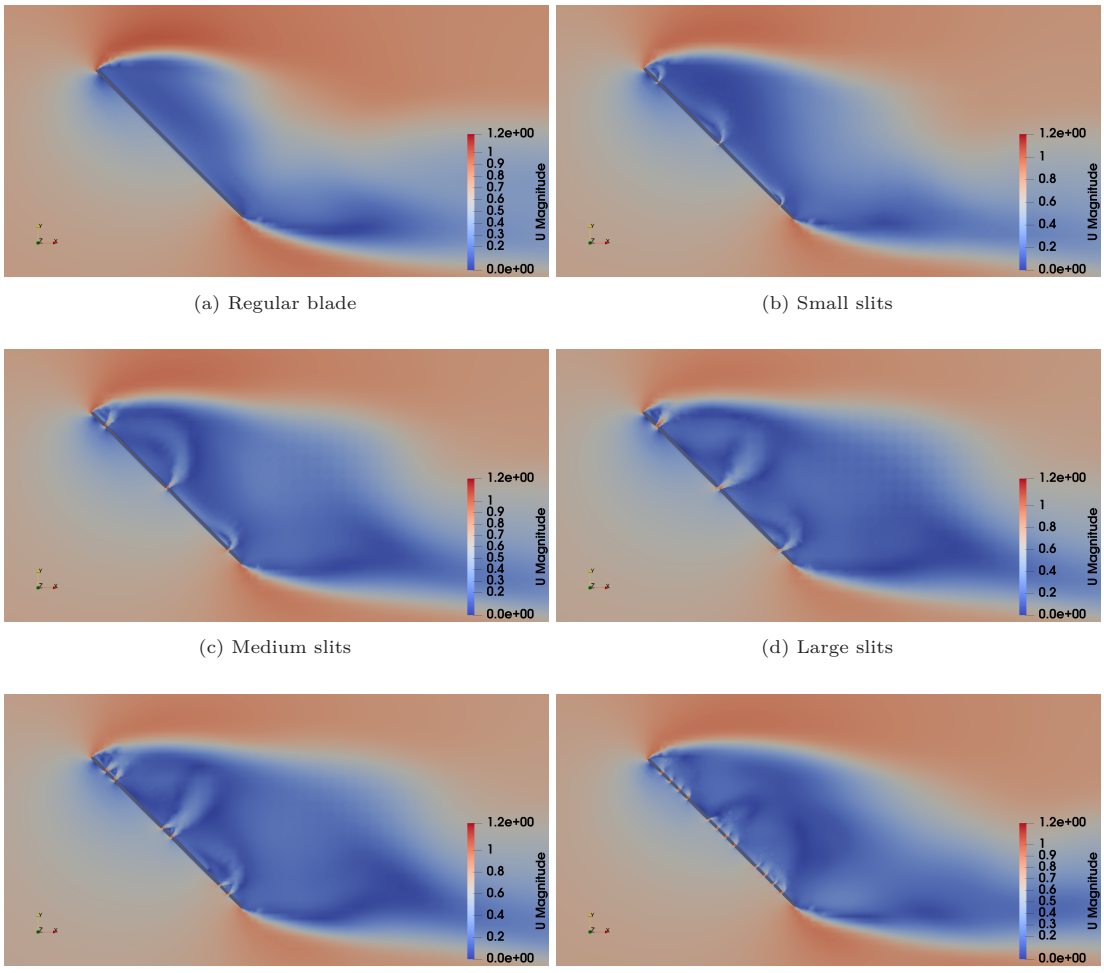

(a) Regular blade

(b) Small slits

(c) Medium slits

(d) Large slits

(e) 12 Slits

(f) 24 slits

Figure 4.8: Velocity distribution near the blade and wake for the different configurations at $\alpha = 45°$.

Blade configuration	Regular	SS	MS	LS	12S	24S
C_D	0.946	0.938	0.918	0.908	0.905	0.874
C_L	0.959	0.922	0.901	0.892	0.858	0.767
y^+_{mean}	0.289	0.270	0.279	0.282	0.286	0.271

Table 4.4: C_D, C_L and corresponding y^+-values for blade held at 45 AOA.

4.5 90 AOA

The results for the blades at 90° angle of attack can be seen in Figure 4.9. The lift values are not included as they are negligibly small. The drag coefficient differ with the minimum drag coefficient found for the LS configuration and the regular blade at approximately 1.63. Drag maximum was obtained for the 24S configuration reaching a value of approximately 1.67. Thus the greatest difference for the drag coefficient amounted to a 2% increase. This is less substantial than the decreases in the coefficients found for the 45 AOA cases. Table 4.5 shows the coefficients with corresponding y^+ values. Velocity magnitude for the flow fields for the six cases are shown in Figure 4.10

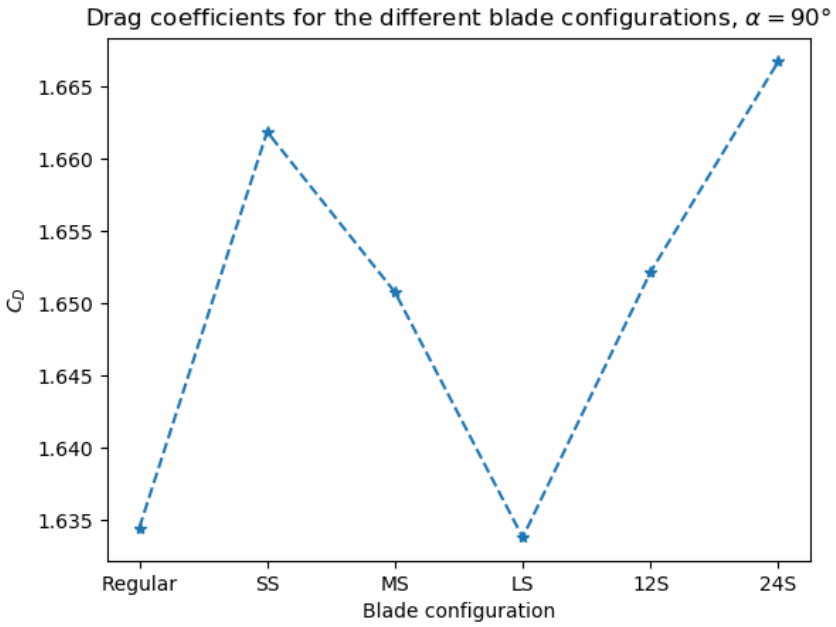

Figure 4.9: Drag coefficients for the different blade configurations held at 90 AOA.

Similarly to the cases at 45AOA we see the flow penetrating the slits. The separation points around each end of the blade are not seen to be affected by the presence of the slits. The ranges in velocity magnitude bar seen on the corner of each image differ between the cases.

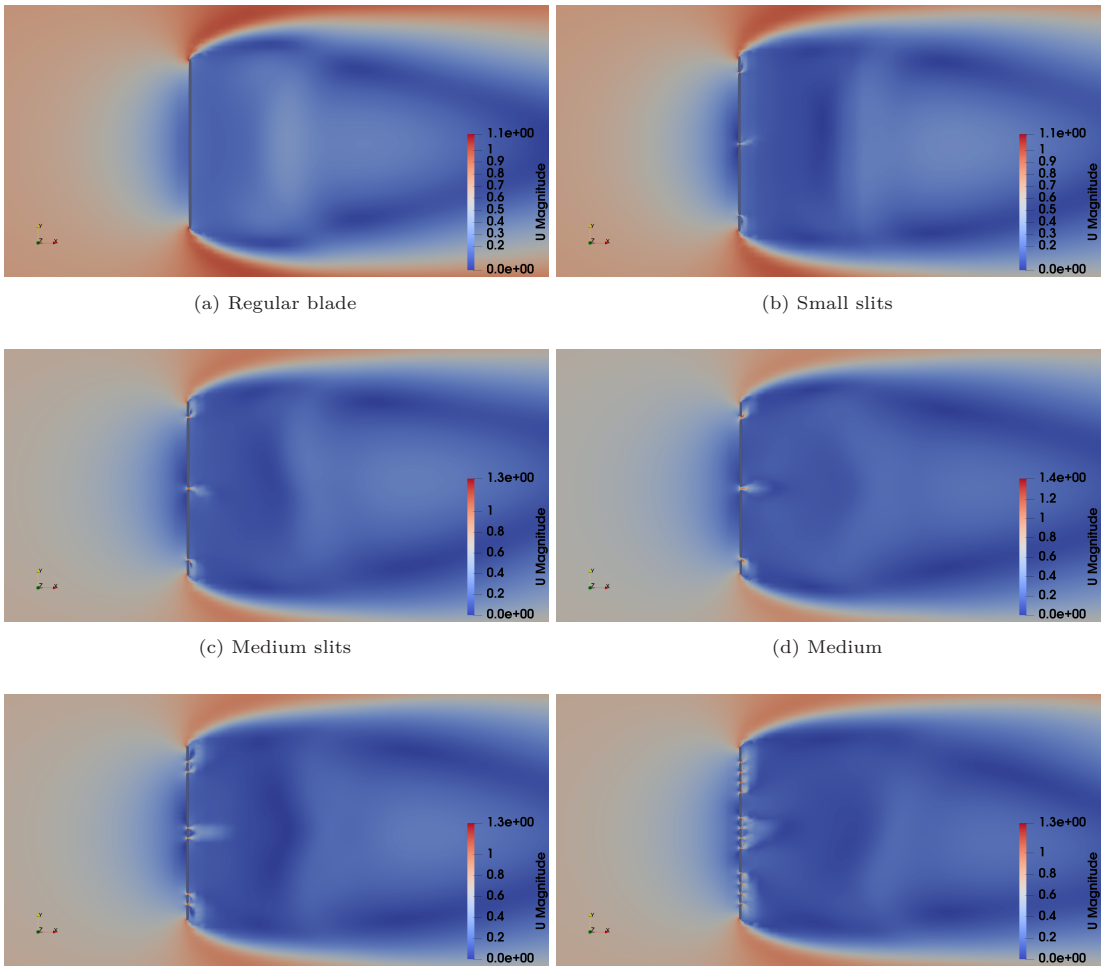

(a) Regular blade

(b) Small slits

(c) Medium slits

(d) Medium

(e) 12 Slits

(f) 24 slits

Figure 4.10: Velocity distribution near the blade and wake for the different configurations at $\alpha = 90°$.

Blade configuration	Regular	SS	MS	LS	12S	24S
C_D	1.635	1.661	1.651	1.634	1.652	1.667
C_L	0.000	0.000	0.000	0.000	0.000	0.000
y^+_{mean}	0.99	0.155	0.632	0.632	0.294	0.951

Table 4.5: C_D, C_L and corresponding y^+-values for blade held at 90 AOA.

4.6 115 AOA

An example of the 3D flow characteristics induced by the 24S configuration is visualized in Figure 4.11. The streamlines reveal vortices behind the slits of the blade. Lastly, the results for 115 angle of attack is shown in Figure 4.12 and Figure 4.13. The findings show an opposite effect of the slits between the drag and lift coefficients. The 24S configuration yielded the largest drag coefficient at approximately 1.40. Compared to the regular blade this configuration saw an approximate increase of 2%. The lift coefficients saw a steeper decrease when compared to the regular blade (lift coefficient 0.64), with the 24S configuration having a lift coefficient of 0.58, a 9 % decrease. The flow visualizations for all configurations are shown in Figure 4.14. The flow characteristics are visually similar as compared with the other angles of attack. Table 4.6 shows the values with corresponding y^+ values.

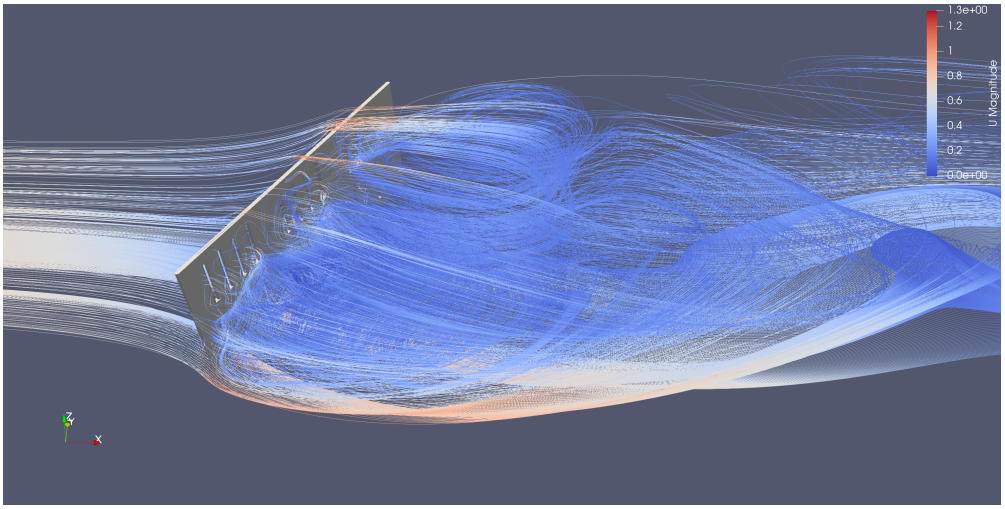

Figure 4.11: The streamlines of the 24S blade over an 115 AOA.

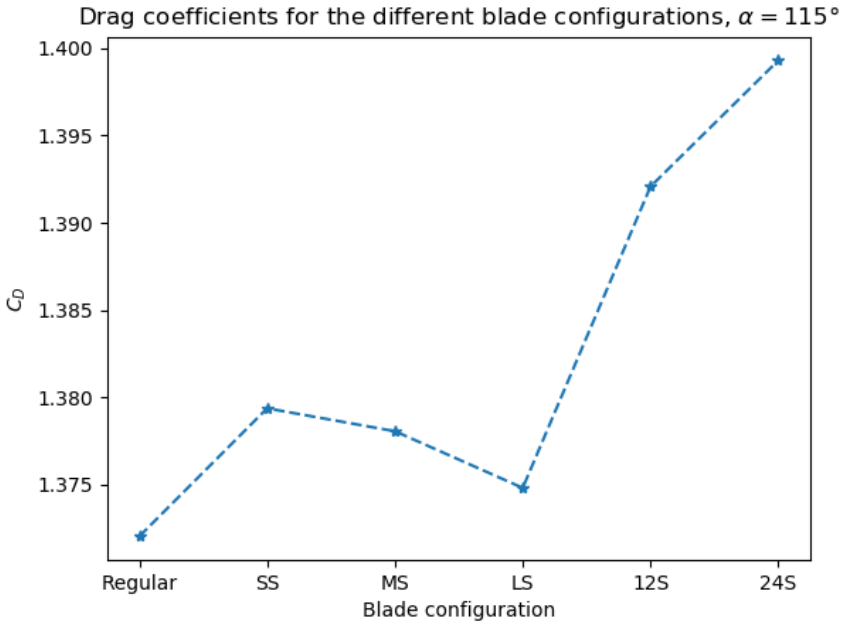

Figure 4.12: Drag coefficients for the different blade configurations held at 115 AOA.

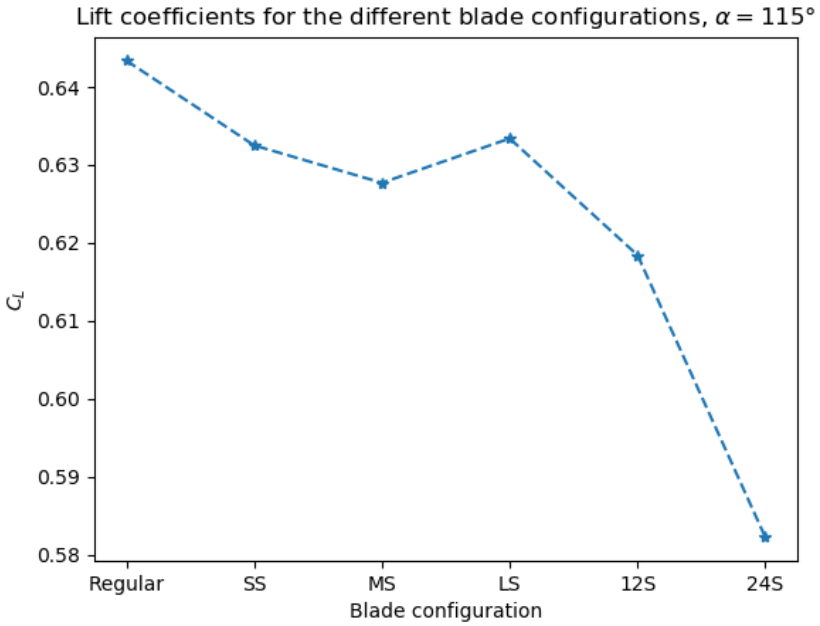

Figure 4.13: Lift coefficients for the different blade configurations held at 115 AOA. Measured in absolute value

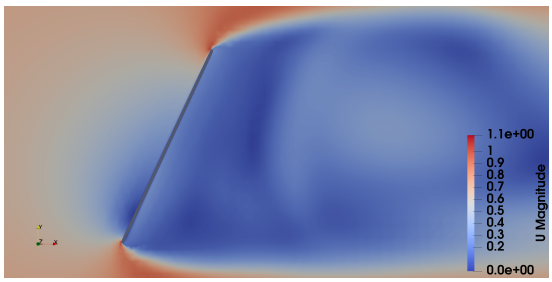

(a) Regular blade

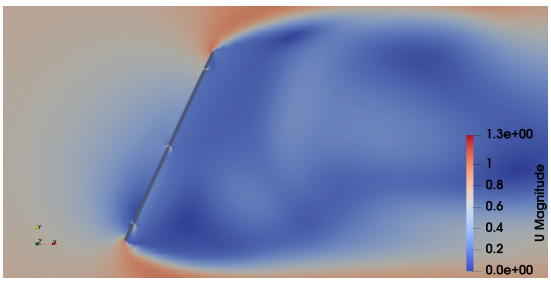

(b) Small slits

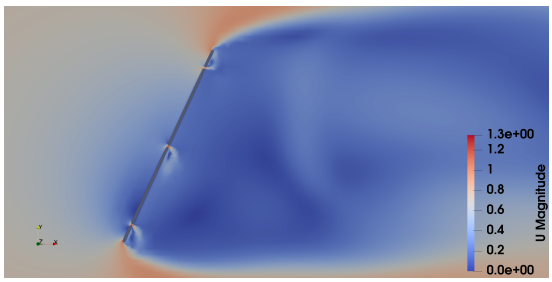

(c) Medium slits

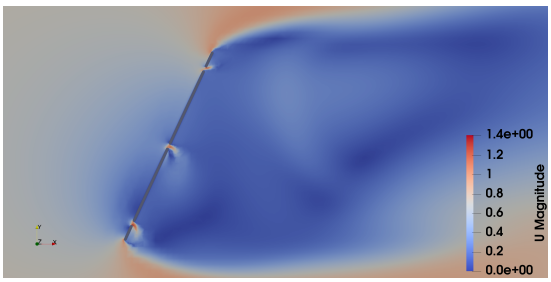

(d) Large slits

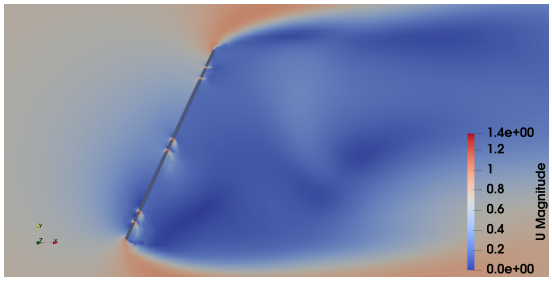

(e) 12 Slits

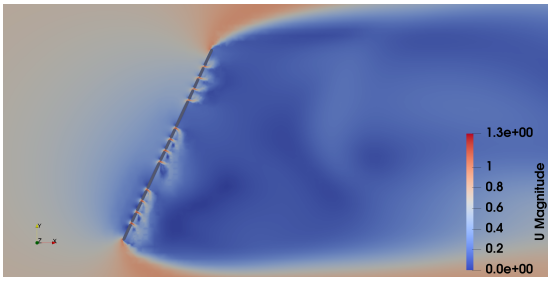

(f) 24 slits

Figure 4.14: Velocity distribution near the blade and wake for the different configurations at $\alpha = 115°$.

Blade configuration	Regular	SS	MS	LS	12S	24S
C_D	1.372	1.379	1.378	1.375	1.392	1.399
$\lvert C_L \rvert$	0.641	0.630	0.625	0.630	0.618	0.582
y^+_{mean}	0.274	0.273	0.273	0.273	0.273	0.272

Table 4.6: C_D, the absolute value of C_L and corresponding y^+-values for blade held at 115 AOA.

CHAPTER 5

Discussion

The discussion will be divided into four sections; First, we make a short summary of our findings. Second, we compare our model results to benchmark evaluations and we interpret the new findings in context with the published literature. Third, we list potential limitations and points for improvement for the present study. Finally, we make conclusions and give a path for future studies on the subject.

5.1 Main findings

In this study, we compared rowing blades with and without slits. We found flow field characteristics to be affected by even the smallest slit configuration used in this study. In general, lift coefficients decreased substantially with increased number of slits and slit size, but the relative decrease depended on the angle of attack. Drag coefficients remained relatively stable, and no clear pattern was seen with different blade configurations.

5.2 Comparison with the literature

The current CFD models ability to predict the drag coefficient for the regular blade showed a good trend, but the drag force coefficients were, as mentioned, underpredicted by a constant. Similarly, underprediction was found for the magnitude of the lift coefficients, although not by a constant. Drag coefficients were underestimated in a range of 15-25 % decrease depending on AOA, while lift was underestimated by a range of 13-27 %.

By comparing the current model with other similar models some insights on model efficacy can be obtained. There are two other CFD studies that have directly compared the experimental studies by Caplan and Gardner to their CFD calculations. The study by Sliasas and Tullis (2009) found good agreement between their CFD simulations and the experimental values, but also found a slight decrease in the coefficients with the larges discrepancy at 45 AOA with a 20% decrease for the drag coefficient and a 14% decrease for the lift coefficient. At 90 AOA they found better agreement with only a 5% decrease in the drag coefficient. They did not model 115 AOA, but at 120 AOA they found a 14% decrease in the drag coefficient and an 8 % decrease in the lift coefficients absolute value. A notable difference between Sliasas and Tullis (2009) and the current study is the treatment of the free surface, where the

former used volume of fluid (VOF) method for defining a multi-phase flow while the current study used the symmetry condition approach.

The other study that has compared the experimental values with CFD is Coppel et al. (2010). This study modeled the free surface by usage of the symmetry condition, similarly to the current study. Coppel et al. (2010). overpredicted the force coefficients compared to the experimental values. The drag coefficient saw a 16% increase at 45 AOA while the lift saw an 11% increase with this angle. At 90 AOA a 32% increase was seen for the drag coefficient, and for the drag and lift coefficients at 115 AOA a 37% and 7% increase was seen, respectively.

All over the best prediction was obtained from the multiphase flow VOF free surface treatment used by Sliasas and Tullis. This indicates that simplifying the free surface through the usage of the symmetry boundary condition decreases model performance.

For the comparison between the regular blades and the blades with slits, differences are found in the force coefficients between the different blade configurations to depend on the angle of attack. Most notable is the decrease in the lift coefficients. The general trend here shows reduced lift coefficient with reduced total area of the blades. The most substantial difference was found between the regular blade and the 24S blade at 45 AOA with a 20% a decrease for the 24S blade. Other findings are some drag increase seen for some cases, although quite small with the largest increase seen at around 2% between the 24S case and the regular blade held at 90 AOA. The smallest differences generally for both coefficients was found for the SS blade and the regular blade with most notably a 2% increase for 90 AOA in the drag coefficient and a 4% decrease in the lift coefficient at 45 AOA.

A significant decrease in lift coefficients is indicative of reduced propulsive force in rowing. As shown in Grift, Tummers and Westerweel (2021), propulsion in rowing is approximately 40% lift induced, being a crucial contributor to propulsion during the early and late stages of the drive phase of the rowing stroke described in Section 1.3. A caveat to this is that it is uncertain how the variations in drag and lift coefficients found in the current study, especially when small, will play out in realistic rowing conditions. One reason for this uncertainty is that studies have shown that the force coefficients in an unsteady rowing blade scenario compared to a quasi-static steady state model differ substantially (Leroyer et al. 2010; Robert, Leroyer, Barré, Rongère et al. 2014).

The inclusion of the slits was believed to increase propulsion in rowing by mimicking finger spacing in swimming. Some of the studies in swimming focuses solely on the drag coefficient when studying this effect (Darázs and Paál 2016; Minetti, Machtsiras and Masters 2009). However, as with rowing, the relative lift-drag contribution in swimming propulsion is believed to vary during the different phases of the swimming stroke (Gourgoulis et al. 2008). Vilas Boas et al. (2015) argues that lift coefficient plays a substantial role in swimming propulsion, although it is not quantified how much. Vilas Boas et al. (2015) tested different hand models through different angles and measured how finger spacing affected the drag and lift coefficients. It was reported that during the drag dominated phase (i.e. the pull) of the swimming stroke, an increase in drag was seen with a slight finger spread. The drag dominated phase in swimming (the pull) corresponds to the middle phase of rowing, and may thus in theory be comparable to our results with 90 AOA. However, the drag coefficients found

for 90 AOA remained relatively constant. Vilas Boas et al. (2015) also noted that the lift coefficient was much less sensitive to this slight spread, showing very similar values compared with no spread during different phases of the swimming stroke. In contrast, almost all the simulation results from the present study suggested that lift coefficients decreased with increased open blade area. Similar findings have been reported in Marinho et al. (2010). This study was conducted similarly to the current rowing blade study. They evaluated drag and lift coefficients with CFD by using a stationary hand model for different finger spacing variations with different AOA. The largest increase found was for the drag coefficient at 45 AOA. In constrast to the findings of our study, where drag was reduced by 7 % when slits were included, Marinho et al. (2010) found a 14 % increase with some finger spread when compared to a closed hand (no finger spread). Additionally, they found the differences in the lift coefficient for different AOA between some finger spread and no spread to be negligibly small. This is also contrary to the present study, where lift was reduced by a maximum of 20 % between the different configurations. The findings by Marinho et al. (2010) and Vilas Boas et al. (2015) can be related to the current study by how finger spread affects drag and lift coefficients differently, as this was also found in the current study with slits in rowing blades. However, there are obvious differences in blade versus hand geometry, and finger spacing do not correspond perfectly to slits included in rowing blades.

5.3 Limitations

Some limitations have already been mentioned concerning the models applicability to a real world rowing scenario and to accurately capture the velocity changes and free surface interactions. This section will outline some additional limitations.

Turbulence model Turbulence modeling with the two-equations models yields limited accuracy depending on the application. The current simulations resembles flow over inclined and normal flat plates which are characterised by separation and complex vortex shedding patterns (Teimourian, Yazdi and Hacisevki 2018). This is not a trivial modeling problem, and consequently force and field calculations are prone to errors.

Reference data Although regular rowing blades are extensively modeled by the studies mentioned, a lack of reference studies for the slit configurations makes the evaluation of the results difficult. The closest comparisons found are with the finger spacing swimming studies, but the the geometries in these cases are not similar.

Geometry implementation The rowing blades modeled were flat rectangular plates with comparative dimension to the most commonly used rowing blade, the "big blade". These have curvature. Curvature effects was not taken into account in the current study. Additionally, all slit sizes tested here are larger than the slits used in e.g. the Oscar blades. In the simulations, slit size $\geq$ 0.6 mm in, while the Oscar blades have slits of less than 0.5 mm on a full scale blade as opposed to a quarter scale blade tested in this study.

Velocity In the current study, we only used one particular steady state velocity. Greater confidence in the findings could be achieved by testing for a range of different velocities. This would be more realistic as the velocity varies throughout the stroke.

5.4 Conclusion

The goal of this thesis was to evaluate whether slits in a rowing blade would increase drag and/or lift coefficients. For most cases, the opposite effect of inclusion of slits were found. The results from the present study do not suggest that the inclusion of slits in blades is recommended. However, our conclusion is based on results from a simplified geometry in static conditions. Different configurations in more dynamic scenarios for closer resemblance to real rowing may gain further insights. Corresponding results from swimming studies suggest that slits in blades with other configurations not included in the present study (e.g. curvature, slit geometry) may increase lift and drag coefficients and thus increase propulsive rowing forces.

Appendices

The CFD codes used for the rowing blade simulations can be found on the following github page:

https://github.com/sverrevi/OpenFOAM/

Bibliography

Alfonsi, G. (2009). 'Reynolds-averaged Navier–Stokes equations for turbulence modeling'. In: *Applied Mechanics Reviews* vol. 62, no. 4.

Almohammadi, K. M. et al. (2012). 'CFD sensitivity analysis of a straight-blade vertical axis wind turbine'. In: *Wind Engineering* vol. 36, no. 5, pp. 571–588.

Baudouin, A. and Hawkins, D. (2004). 'Investigation of biomechanical factors affecting rowing performance'. In: *Journal of biomechanics* vol. 37, no. 7, pp. 969–976.

Boussinesq, J. (1877). 'Theorie de l'ecoulement tourbillant'. In: *Mem. Acad. Sci.* vol. 23, p. 46.

Caplan, N. and Gardner, T. (2007). 'Modeling the influence of crew movement on boat velocity fluctuations during the rowing stroke'. In: *International Journal of Sports Science and Engineering* vol. 1, no. 3, pp. 165–176.

Caplan, N. and Gardner, T. N. (2007). 'A fluid dynamic investigation of the Big Blade and Macon oar blade designs in rowing propulsion'. In: *Journal of sports sciences* vol. 25, no. 6, pp. 643–650.

Chen, C. J. (1997). *Fundamentals of turbulence modelling*. CRC Press.

Chen, J. M. and Fang, Y.-C. (1996). 'Strouhal numbers of inclined flat plates'. In: *Journal of wind engineering and industrial aerodynamics* vol. 61, no. 2-3, pp. 99–112.

Coppel, A. et al. (2010). 'Simulating the fluid dynamic behaviour of oar blades in competition rowing'. In: *Proceedings of the Institution of Mechanical Engineers, Part P: Journal of Sports Engineering and Technology* vol. 224, no. 1, pp. 25–35.

Darázs, B. D. and Paál, G. (2016). 'Optimum finger spacing for swimmers'. In: *Periodica Polytechnica Mechanical Engineering* vol. 60, no. 1, pp. 1–14.

Eça, L., Pereira, F. and Vaz, G. (2018). 'Viscous flow simulations at high Reynolds numbers without wall functions: Is y+= 1 enough for the near-wall cells?' In: *Computers & Fluids* vol. 170, pp. 157–175.

Gourgoulis, V. et al. (2008). 'Estimation of hand forces and propelling efficiency during front crawl swimming with hand paddles'. In: *Journal of Biomechanics* vol. 41, no. 1, pp. 208–215.

Grift, E., Tummers, M. and Westerweel, J. (2021). 'Hydrodynamics of rowing propulsion'. In: *Journal of Fluid Mechanics* vol. 918.

Houwelingen, J. van et al. (2017). 'The effect of finger spreading on drag of the hand in human swimming'. In: *Journal of biomechanics* vol. 63, pp. 67–73.

Jasak, H. (1996). 'Error analysis and estimation for the finite volume method with applications to fluid flows.' In:

Kleshnev, V. (1999). 'Propulsive efficiency of rowing'. In: *ISBS-Conference Proceedings Archive*.

— (2020). *Biomechanics of Rowing: A unique insight into the technical and tactical aspects of elite rowing*. The Crowood Press.

Kok, J. C. (2000). 'Resolving the dependence on freestream values for the k-turbulence model'. In: *AIAA journal* vol. 38, no. 7, pp. 1292–1295.

Launder, B. and Spalding, D. (1974). 'The numerical computation of turbulent flows'. In: *Computer Methods in Applied Mechanics and Engineering* vol. 3, no. 2, pp. 269–289.

Leroyer, A. et al. (2010). 'Influence of free surface, unsteadiness and viscous effects on oar blade hydrodynamic loads'. In: *Journal of Sports Sciences* vol. 28, no. 12, pp. 1287–1298.

Lorente, S. et al. (2012). 'The constructal-law physics of why swimmers must spread their fingers and toes'. In: *Journal of theoretical biology* vol. 308, pp. 141–146.

Marinho, D. A. et al. (2010). 'Swimming propulsion forces are enhanced by a small finger spread'. In: *Journal of Applied Biomechanics* vol. 26, no. 1, pp. 87–92.

Martin, T. P. and Bernfield, J. S. (1980). 'Effect of stroke rate on velocity of a rowing shell.' In: *Medicine and science in sports and exercise* vol. 12, no. 4, pp. 250–256.

Menter, F. R. (1994). 'Two-equation eddy-viscosity turbulence models for engineering applications'. In: *AIAA journal* vol. 32, no. 8, pp. 1598–1605.

Menter, F. R., Kuntz, M. and Langtry, R. (2003). 'Ten years of industrial experience with the SST turbulence model'. In: *Turbulence, heat and mass transfer* vol. 4, no. 1, pp. 625–632.

Minetti, A. E., Machtsiras, G. and Masters, J. C. (2009). 'The optimum finger spacing in human swimming'. In: *Journal of biomechanics* vol. 42, no. 13, pp. 2188–2190.

Narasimhamurthy, V. D. and Andersson, H. I. (2009). 'Numerical simulation of the turbulent wake behind a normal flat plate'. In: *International Journal of Heat and Fluid Flow* vol. 30, no. 6, pp. 1037–1043.

Oberkampf, W. L. and Trucano, T. G. (2002). 'Verification and validation in computational fluid dynamics'. In: *Progress in aerospace sciences* vol. 38, no. 3, pp. 209–272.

Patankar, S. V. and Spalding, D. B. (1983). 'A calculation procedure for heat, mass and momentum transfer in three-dimensional parabolic flows'. In: *Numerical prediction of flow, heat transfer, turbulence and combustion*. Elsevier, pp. 54–73.

Pulman, C. (2005). 'The physics of rowing'. In: *University of Cambridge*, pp. 1–7.

Reynolds, O. (1895). 'IV. On the dynamical theory of incompressible viscous fluids and the determination of the criterion'. In: *Philosophical transactions of the royal society of london.(a.)*, no. 186, pp. 123–164.

Robert, Y., Leroyer, A., Barré, S., Queutey, P. et al. (2019). 'Validation of CFD simulations of the flow around a full-scale rowing blade with realistic kinematics'. In: *Journal of Marine Science and Technology* vol. 24, no. 4, pp. 1105–1118.

Robert, Y., Leroyer, A., Barré, S., Rongère, F. et al. (2014). 'Fluid mechanics in rowing: the case of the flow around the blades'. In: *Procedia Engineering* vol. 72, pp. 744–749.

Secher, N. H. and Volianitis, S. (2009). *The Handbook of Sports Medicine and Science: Rowing*. John Wiley & Sons.

Sidelnik, N. and Young, B. (2006). 'Optimising the freestyle swimming stroke: the effect of finger spread'. In: *Sports Engineering* vol. 9, no. 3, pp. 129–135.

Sliasas, A. and Tullis, S. (2009). 'Numerical modelling of rowing blade hydrodynamics'. In: *Sports Engineering* vol. 12, no. 1, pp. 31–40.

Teimourian, A., Yazdi, S. G. and Hacisevki, H. (2018). 'Vortex shedding: a review on flat plate'. In: *Fluid Dynamics* vol. 53, no. 2, pp. 212–221.

Versteeg, H. K. and Malalasekera, W. (2007). *An introduction to computational fluid dynamics: the finite volume method*. Pearson education.

Vilas Boas, J. P. et al. (2015). 'Hydrodynamic analysis of different finger positions in swimming: a computational fluid dynamics approach'. In: *Journal of applied biomechanics* vol. 31, no. 1, pp. 48–55.

White, F. M. and Majdalani, J. (2006). *Viscous fluid flow*. Vol. 3. McGraw-Hill New York.

Wilcox, D. (1991). 'A half century historical review of the k-omega model'. In: *29th Aerospace Sciences Meeting*, p. 615.

Wilcox, D. C. (1988). 'Reassessment of the scale-determining equation for advanced turbulence models'. In: *AIAA journal* vol. 26, no. 11, pp. 1299–1310.

Yusuf, S. N. A. et al. (2020). 'A short review on rans turbulence models'. In: *CFD Letters* vol. 12, no. 11, pp. 83–96.